UNIVERSITÀ DEGLI STUDI DI PADOVA

Dipartimento di Fisica e Astronomia "Galileo Galilei"

Master Degree in Physics

Final Dissertation

Iron-doped Lithium Niobate thin films on GaN: fabrication and characterization

Thesis supervisor

Dr. Marco Bazzan

Candidate

Paolo Andrea Wetzl

Academic Year 2019/2020

Paolo Andrea Wetzl:
Iron-doped Lithium Niobate thin films on GaN: fabrication and characterization
July 2020

ABSTRACT

In recent time ferroelectric thin films have attracted significant attention due to the observation of several phenomena that manifest in new and intriguing ways. This is the case of photogalvanic effect, also known as bulk photovoltaic effect (BPVE), consisting in the spontaneous onset of a small electrical current when a polar material is illuminated with a uniform light. A precise understanding of this effect could possibly lead to new applications, in particular in the field of photovoltaics. In fact, as the mechanism of charge separation is completely different, those materials are not a priori bounded by the theoretical Shockley–Queisser limit which applies to standard photovoltaic devices such as p-n junctions in semiconductors.

In spite of this, the use of BVPE for photovoltaic energy conversion is limited by the smallness of the photogenerated current. In an effort to improve this aspect, a proposal has been made to use nano-sized materials because in this case photogenerated charges could be extracted more efficiently from the ferroelectric. In particular, iron-doped Lithium Niobate (Fe:LN) is one of the best known photogalvanic materials and is therefore the ideal playground to test this approach, namely evidence an increase of the BVPE upon reducing the crystal size to the nanoscale.

Unfortunately, lithium niobate has an intrinsically defective structure and its electrical properties are strongly affected both by its composition and its structural properties, such as strain etc. A precise knowledge of the film composition and structure is thus mandatory in order to set the ground for forthcoming investigations. For this reason, in this work we undergo the task of characterizing a set of Fe:LN thin films epitaxially grown on GaN substrates on different conditions by RF-Magnetron sputtering. This activity, carried out in collaboration with Università Ca' Foscari (Venezia) and Laboratori Nazionali di Legnaro (LNL-INFN) is based on a combination of techniques and protocols developed here for this specific kind of samples. The techniques used are HR-XRD, RBS, NRA and UV-Vis optical absorption spectroscopy. The results show that the produced samples are characterized by a marked Li deficiency and a structural compressive strain determined by the epitaxial relation with the substrate and provide useful indications on how to improve the deposition parameters.

CONTENTS

ACRONYMS

BPVE Bulk PhotoVoltaic Effect

LN Lithium Niobate

cLN Congruent Lithium Niobate

sLN Stoichiometric Lithium Niobate

SC Smart Cut

AFM Atomic Force Microscopy

HR-XRD High-Resolution X-Ray Diffractometry

RBS Rutherford Backscattering Spectrometry

NRA Nuclear Reaction Analysis

RSM Reciprocal Space Map

RFMS Radio Frequency Magnetron Sputtering

TMM Transfer Matrix Method

RMS Root Mean Square

1

INTRODUCTION

Photovoltaic effect can be broadly defined as the production of a voltage difference triggered by light absorption. The study of photovoltaic effect has gained growing attention in the last decades as its most prominent application, solar energy harvesting photovoltaic cells, are believed to be crucial to satisfy our energy needs in the future.

Photovoltaic cells are devices designed to harness energy from photons, mainly in the visible range, by converting them to an electrical current by means of the photovoltaic effect. In such devices, three steps are needed to convert the photon's energy into electrical power. Photons must be absorbed by the material and they must form charge carriers, such as electron-hole pairs, excitons or polaron pairs. These carriers tend to recombine and disappear from the materials, transforming the absorbed energy into heat. For this reason the photogenerated charge carriers must be separated and extracted from the cell to an external circuit for use of the generated electrical power.

The most common type of photovoltaic cells are based on the p-n junction. In such devices, the incoming photon excites inside the junction volume an electron from valence band to the conduction band, thus generating an electron-hole pair. Because of the junction design, the electric field at the depletion zone separates the photo-generated charge carriers on opposite sides of the junction for collection by electrodes.

A famous study on the efficiency of photovoltaic cells based on this design was performed by Shockley and Queisser in 1961 by taking into account many sources of energy losses such as thermal radiation emission, charge carrier recombination and spectrum losses due to the fact that photons having energy smaller than the material's band gap are unable to excite electrons from the valence to the conduction band. The maximum theoretical power conversion efficiency for such cell

type is found to be 33.7% at 1.34 eV and is called the Shockley-Queisser limit. [1]

The race for power conversion efficiencies higher than the Shockley-Queisser limit has motivated research in new materials and strategies.

A common feature of photovoltaic effect in p-n junctions as a consequence of the Shockley-Queisser limit is that the maximum open-circuit voltage, that is the voltage measured in the crystal in an open-circuit configuration under illumination, is limited by the material's band gap. A class of ferroelectric crystals shows a peculiar kind of photovoltaic effect with several differences from the conventional one, such as open-circuit voltages as high as several kV for mm-thick crystals, which are largely above the band-gap. Moreover this phenomenon originates intrinsically in the bulk of the material and is not due to the presence of a junction. For these reasons this effect is called *Anomalous* or *Bulk Photo-Voltaic Effect* (BPVE). This effect arises from an asymmetry in the generation or transport of the photogenerated charges, owing to the non-centrosymmetric nature of the ferroelectric crystals.

Despite the high open circuit photovoltages, power conversion in these materials is still low, due to the charge transport mechanisms in such materials, which involves photoexcited polaron carriers moving a few lattice sites at the time. A possible solution to increase power conversion would be to reduce the system's size to the nanoscale, by synthesizing crystalline thin films. Promising results in this direction have been found in recent years for $BaTiO_3$ thin films. [2] More recently it was also reported an increase in BPVE due to moderate strain in Fe:$LiNbO_3$ bulk crystals, which suggests that an even higher increases could be found in thin films, which are affected by higher strain. [3]

In the last ten years research has advanced in the understanding of photovoltaic effects in ferroelectric materials and power conversion efficiency has significantly improved. [4] Due to the significant differences in the photovoltaic process compared to conventional materials, the maximum power conversion limit has not been yet understood and could possibly lead to a surpassing of the Shockley-Queisser limit.

This thesis work is part of a research project aimed to studying BVPE in Fe:$LiNbO_3$ nanofilms. One of the problems to be solved concerns the fabrication of the films, which have to be of high crystalline quality not to spoil the BPVE and electrically connected to two electrodes on the positive and negative ferroelectric surfaces. We developed a bottom-up approach in which the Fe:$LiNbO_3$ films are grown on a doped GaN substrate which will work both as an epitaxial surface and as an electrical contact. The goal of this thesis work is to assess the crystal quality and composition of the produced films before proceeding with photoelectrical characterization in future works.

2

STATE OF THE ART

2.1 LITHIUM NIOBATE

Several ferroelectric materials show Bulk Photovoltaic Effect (BPVE). Our choice is to focus on lithium niobate ($LiNbO_3$) a perovskite which has been widely studied in the past 60 years and that is readily available in high quality crystals, also due to the extensive use in telecommunication devices.

Its photovoltaic properties have already been extensively studied iron-doped bulk specimens. [5]

Lithium niobate ($LiNbO_3$, often labeled as *LN*) is a synthetic material, first studied in 1928 by Zachariasen, discovered as ferroelectric in 1949 by Matthias and Remeika at Bell Laboratories, where it was widely investigated by Nassau and Abrahams, which led to five papers published in 1966. [6]

It is colorless, chemically stable and insoluble in water and in organic solvents. It has a high melting point, around 1528 K [7].

It is a dielectric and ferroelectric material, whose advantageous physical properties have been studied and tuned for the design of electro-optic and acousto-optic devices.

2.1.1 *Crystal structure*

Lithium niobate is a ABO_3 ferroelectric perovskite, in the same displacement ferroelectrics family of other materials such as $LiTaO_3$ and $BaTiO_3$. The material has a ferroelectric phase at temperatures below its Curie temperature, which is around 1483 K. Its structure consists of planar sheets of oxygen atoms, in a distorted hexagonal closed packed structure. The octahedral interstices formed in such structure are equally filled either by lithium, niobium atoms or are vacant, with a one third occupancy each. Moving perpendicular to the oxygen

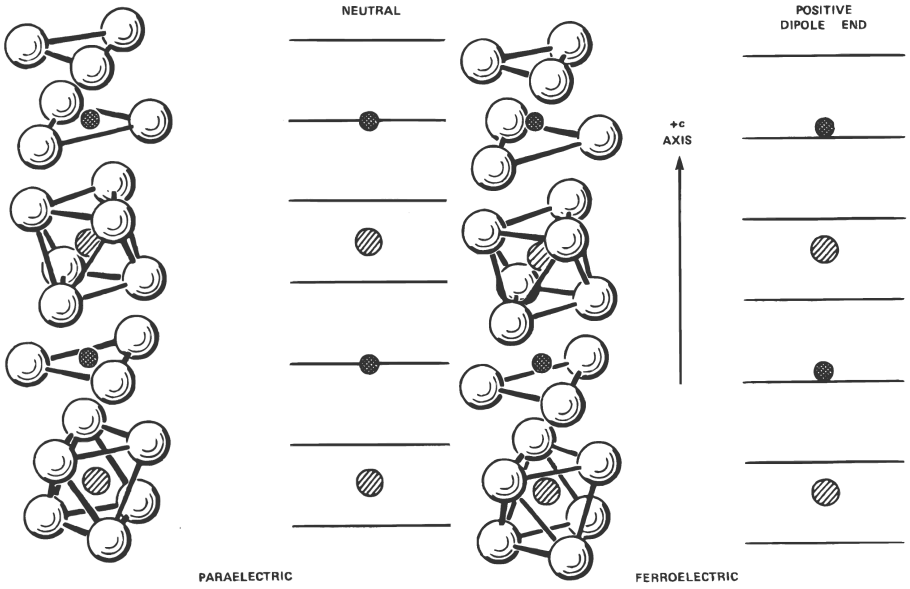

Figure 2.1: Positions of the Li and Nb atoms in the paraelectric (left) and ferroelectric (right) phases of $LiNbO_3$. White circles represent the O atoms, single cross-hatched circles Nb atoms while double cross-hatched ones represent Li atoms. From [6]

hexagonal planes, the atoms in the interstitial positions are filled in the following order: Li, Nb, vacancy, Li, Nb, vacancy. This direction is commonly referred as $+c$ or $+z$ direction and represents the polar direction of the crystal.

In the paraelectric phase, above the Curie temperature, the Li atoms lie in oxygen hexagonal planes, while the Nb atoms lie at the center of the oxygen octahedrals, at the center between the second and third next oxygen planes from Li atoms. In this configuration, the crystal is non polar. As temperature decreases below the Curie temperature, a different configuration is reached, where both Li and Nb atoms are shifted from oxygen planes in the same c direction, breaking the symmetry and resulting in a spontaneous polarization along this direction.

This crystal in the ferroelectric phase shows a three-fold rotational symmetry about a c axis, perpendicular to the hexagonal oxygen planes described previously, and is therefore a member of the trigonal crystal system. It also shows mirror symmetry about three planes separated by a 60° angle, whose intersection is the three-fold rotation axis c. For these reasons $LiNbO_3$ is classified as a member of the $3m$ point group. Additionally it belongs to the $R3c$ space group. [6]

To describe a trigonal system, two types of unit cells can be used: hexagonal and rhombohedral. In the hexagonal unit cell, the **c** axis is chosen as the three-fold rotational symmetry axis. The positive direction $+\mathbf{c}$ is defined as the direction out of the crystal face which

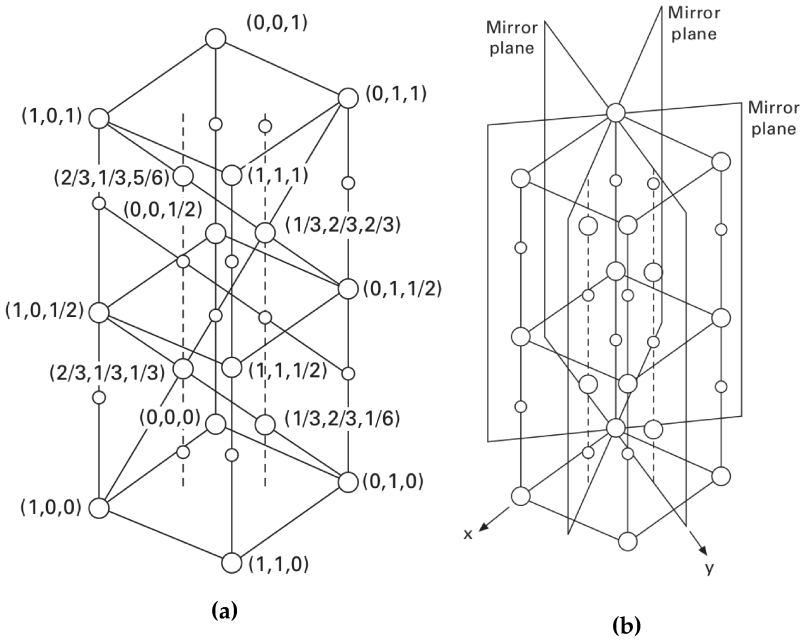

Figure 2.2: Lithium niobate's hexagonal cell schematics with positional coordinates of lithium and niobium atoms indicated (**a)**) or with the three mirror planes associated with $3m$ symmetry (**b)**). Big spheres represent niobium atoms, while smaller ones represent oxygen atoms. From [8].

experiences a negative charge buildup when a uniaxial compression along this axis is performed (piezoelectric effect).

A set of three equivalent axes, $\mathbf{a_1}$, $\mathbf{a_2}$, $\mathbf{a_3}$, is defined in the oxygen hexagonal plane, with the three axes lying 120° apart from each other. Only two of such axes are strictly required for the description of the crystal structure. However, in order to highlight the symmetry of the hexagonal plane, a third one is usually defined. For this reason, a four index Bravais-Miller notation will be used in this thesis (as in the section 4.1, describing the XRD analysis). In such notation, the Miller indices h, k, l and m are related respectively to the $\mathbf{a_1}$, $\mathbf{a_2}$, $\mathbf{a_3}$ and $\mathbf{c}$ axes in this order. The index referred to the extra hexagonal axis is not independent from the two others, but its value is computed as $l = -(h + k)$.

Most of lithium niobate physical properties are expressed through tensors defined on a set of Cartesian coordinates. Such set has the z axis parallel to the $\mathbf{c}$ axis, the x axis is parallel to any of the hexagonal lattice vectors $\mathbf{a_i}$ and the y is chosen perpendicular to the other axes, to form a right hand set. The y axis lies in one of the mirror planes. This enables a method to discover the y face, as upon compression, the $+y$ face becomes negatively charged. This does not happen for the x direction as this axis is perpendicular to a mirror plane and therefore

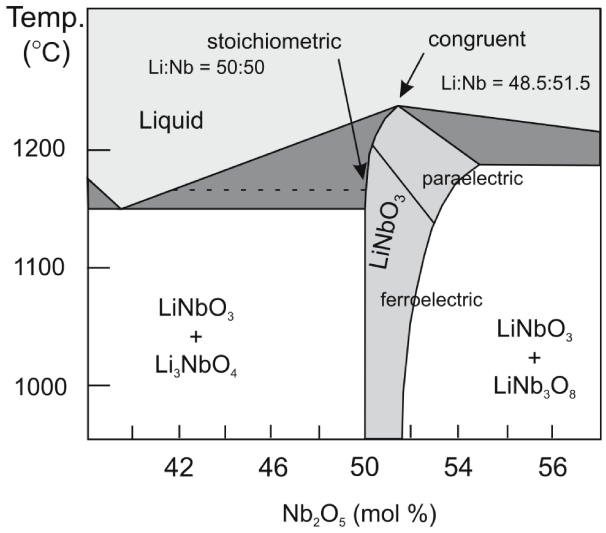

Figure 2.3: Phase diagram of the Li_2O-Nb_2O_5 system. From [7]

every charge movement is mirrored on the other side of the plane and no charge difference can be established.

2.1.2 *Stoichiometric and congruent composition*

Lithium niobate is one of the many compounds obtainable from the binary Li_2O-Nb_2O_5 system. Its phase diagram is reported in Figure 2.3. As we can see, lithium niobate can have a variable composition and it is solid in a wide (6%) range of Li_2O-Nb_2O_5 molar %. Two important crystal compositions are to be noticed in this phase diagram. A segment located at 50% Nb_2O_5 concentration corresponds to the *stoichiometric composition* (sLN), in which the [Li]/[Nb] ratio is 50/50. The liquid-solid curve maximum point at 51.5% Nb_2O_5 concentration corresponds to the *congruent composition* (cLN), a lithium deficient composition with a [Li]/[Nb] ratio of 48.5/51.5.

High-quality lithium niobate single crystals are usually grown from polycrystalline lithium niobate, using Czochralski technique. As in the congruent composition both the melt and the crystal have the same composition, growth with this method results in very uniform crystals, unlike similar growth with different composition, such as stoichiometric one, in which the composition of the melt and the crystal can vary during the growth of the crystal. [7]

Most of lithium niobate's properties are strongly dependent on its composition such as its UV absorption edge, its Curie temperature and its electro-optic coefficient. [7]

2.1.3 *Physical properties*

Many of lithium niobate's properties descend from the displacement of the Li and Nb atoms from their sites, due to external stress. Two examples of such behavior are the pyroelectric and the piezoelectric effects. Lithium niobate being a ferroelectric material also displays a room temperature spontaneous polarization $P_s = 70\,\mu C\,cm^{-1}$ [7].

PYROELECTRIC EFFECT Pyroelectric materials exhibit a change in spontaneous polarization as a function of a temperature variation. The relation between the change in temperature ΔT and the change in spontaneous polarization $\mathbf{\Delta P}$ is linear $\mathbf{\Delta P} = p\Delta T$ or in component form $\Delta P_i = p_i \Delta T$, where p is the pyroelectric tensor. As in lithium niobate this effect is due to the movement of Li and Nb ions, and they are constrained to move parallel to the c direction, the pyroelectric tensor has only one non-zero component, the z component:

$$p = \begin{bmatrix} 0 \\ 0 \\ p_3 \end{bmatrix} \tag{2.1}$$

with $p_3 = -4 \times 10^{-5}\,C/(m^2K)$ [6]. The negative sign of this component indicates that the $+c$ crystal face will become more positively charged upon cooling.

PIEZOELECTRIC EFFECT Piezoelectric materials display an induced polarization as the effect of applied stress. The relation between stress and polarization is linear and can be expressed as $\mathbf{P} = \tilde{d}\,\tilde{\sigma}$ or in tensor component form:

$$P_i = \sum_{j,k} d_{ijk}\sigma_{jk} \tag{2.2}$$

where d_{ijk} is the piezoelectric tensor and σ_{jk} is the stress tensor $i, j, k = x, y, z$, The stress tensor can be shown to be symmetric $\sigma_{jk} = \sigma_{kj}$, resulting in only 6 independent parameters. Therefore a more compact notation can be employed to denominate such components in the stress tensor and in other related tensors such as the piezoelectric tensor. Such convention is called Voigt notation:

$$jk = 11 = 1 \quad 23, 32 = 4 \tag{2.3}$$

$$22 = 2 \quad 31, 13 = 5 \tag{2.4}$$

$$33 = 3 \quad 12, 21 = 6 \tag{2.5}$$

Due to the symmetric nature of the stress tensor, the three rank piezoelectric tensor has only 18 independent elements and can be written as a 3×6 matrix, using Voigt notation to shorten the writing of the jk indices.

Table 2.1: Piezoelectric strain coefficients $[\times 10^{-11}\,\mathrm{C\,N^{-1}}]$.

d_{15}	d_{22}	d_{31}	d_{33}	Ref.
6.92	2.08	−0.085	0.6	[9]
6.8	2.1	−0.1	0.6	[10]
7.4	2.1	−0.087	1.6	[11]

The form of the piezoelectric tensor is determined by the symmetry of the crystal, as prescribed by Neumann's principle which states that all tensors describing physical properties of a crystal must posses at least the symmetry of the crystal. Applying such principle to the lithium niobate crystal, which has $3m$ point symmetry, results in a piezolectric tensor of the form:

$$d_{ijk} = \begin{bmatrix} 0 & 0 & 0 & 0 & d_{15} & -2d_{22} \\ -d_{22} & d_{22} & 0 & d_{15} & 0 & 0 \\ d_{31} & d_{31} & d_{33} & 0 & 0 & 0 \end{bmatrix} \tag{2.6}$$

Symmetry reduces the number of independent parameters to only four coefficients:

Piezoelectric materials also show also a change in their shape (strain) as an electric field is applied, a phenomena known as *converse piezoelectric* effect. It can be shown by a thermodynamic argument that the coefficients relating the applied electric field with the resulting strain are the same connecting the applied stress and the resulting induced polarization in the *direct* piezoelectric effect. The linear response expression for this phenomena can be expressed in tensor form as:

$$S_{jk} = \sum_i d_{ijk} E_i \tag{2.7}$$

where S_{jk} is the second rank strain tensor. [6]

ELASTIC PROPERTIES The elasticity of a solid can be described by the *strain* resulting from an applied *stress*. If the stress is kept within the material's elastic limit, the relationship between stress and strain is linear (Hooke's law) and can be expressed in tensor form as:

$$S_{ij} = \sum_{k,l} c_{ijkl} \sigma_{kl} \tag{2.8}$$

where S_{ij} and σ_{kl} are second-rank strain and stress tensors and c_{ijkl} is the fourth-rank *elastic stiffness* tensor. An inverse relation can be written as:

$$\sigma_{ij} = \sum_{k,l} s_{ijkl} Skl \tag{2.9}$$

where s_{ijkl} is the fourth-rank *elastic compliance* tensor.

Table 2.2: Elastic stiffness coefficients $[\times 10^{11}\,\mathrm{N\,m^{-2}}]$ at constant electric field.

c_{11}	c_{12}	c_{13}	c_{14}	c_{33}	c_{44}	Ref.
2.030	0.573	0.752	0.085	2.424	0.595	[9]
2.03	0.53	0.75	0.09	2.45	0.6	[10]

Table 2.3: Elastic compliance coefficients $[\times 10^{-12}\,\mathrm{m^2\,N^{-1}}]$ at constant electric field.

s_{11}	s_{12}	s_{13}	s_{14}	s_{33}	s_{44}	Ref.
5.831	−1.150	−1.1452	−1.0	5.026	17.10	[9]
5.78	−1.01	−1.47	−1.02	5.02	17.0	[10]

Ignoring body torques it is possible to obtain the following conditions: $s_{ijkl} = s_{ijlk} = s_{jikl}$, which reduce the number of independent elements in both the fourth-rank tensors from 81 to 36 elements. We can write them as 6×6 matrices using Voigt notation. [6]

The crystal's symmetry group, as for Neumann's principle, impose other conditions on the components of the elastic stiffness and compliance tensor, which can be ultimately written as:

$$c_{ijkl} = \begin{bmatrix} c_{11} & c_{12} & c_{13} & c_{14} & 0 & 0 \\ c_{12} & c_{11} & c_{13} & -c_{14} & 0 & 0 \\ c_{13} & c_{13} & c_{33} & 0 & 0 & 0 \\ c_{14} & -c_{14} & 0 & c_{44} & 0 & 0 \\ 0 & 0 & 0 & 0 & c_{44} & c_{14} \\ 0 & 0 & 0 & 0 & c_{14} & \frac{1}{2}(c_{11} - c_{12}) \end{bmatrix} \tag{2.10}$$

$$s_{ijkl} = \begin{bmatrix} s_{11} & s_{12} & s_{13} & s_{14} & 0 & 0 \\ s_{12} & s_{11} & s_{13} & -s_{14} & 0 & 0 \\ s_{13} & s_{13} & s_{33} & 0 & 0 & 0 \\ s_{14} & -s_{14} & 0 & s_{44} & 0 & 0 \\ 0 & 0 & 0 & 0 & s_{44} & 2s_{14} \\ 0 & 0 & 0 & 0 & 2s_{14} & 2(s_{11} - s_{12}) \end{bmatrix} \tag{2.11}$$

Such tensors depend only on 6 independent parameters. In order to determine the value of these coefficients, the contribution of the piezoelectric effect must be taken into account.[8]

When this is properly performed, the elastic stiffness and compliance coefficients are measured, with results reported in Table 2.2 and Table 2.3.

DIELECTRIC PERMITTIVITY Some of the most striking properties of lithium niobate are its optical properties. Lithium niobate is an optical transparent medium, with negligible absorption in the 0.35-3.5 µm

Table 2.4: Stress-free ε^T or strain-free ε^S dielectric relative permittivity coefficients.

$\varepsilon^T_{11}/\varepsilon_0$	$\varepsilon^T_{33}/\varepsilon_0$	$\varepsilon^S_{11}/\varepsilon_0$	$\varepsilon^S_{33}/\varepsilon_0$	Ref.
85.2	28.7	44.3	27.9	[10]
84.1	28.1	46.5	27.3	[12]

range, and its optical properties are sensitive of compositional changes, defects and impurities. This will be employed for the characterization of the iron impurity concentration in the Fe:$LiNbO_3$ thin-films, as explained in section 4.3.

The material's permittivity tensor $\tilde{\varepsilon}$ is defined as the second-rank tensor relating the electric flux density $\mathbf{D}$ and the electric field $\mathbf{E}$: $\mathbf{D} = \tilde{\varepsilon}\mathbf{E}$, or in tensor component form:

$$D_i = \sum_j \varepsilon_{ij} E_j \tag{2.12}$$

where i, j can be x, y, z.

The permittivity tensor is diagonal and, due to the crystal rotational symmetry around the c axis, its components are the same in each direction on the plane perpendicular to that axis, resulting in the following tensor: [6]

$$\varepsilon_{ij} = \begin{bmatrix} \varepsilon_{11} & 0 & 0 \\ 0 & \varepsilon_{11} & 0 \\ 0 & 0 & \varepsilon_{33} \end{bmatrix} \tag{2.13}$$

The material has a large natural birefringence, which can be traced to the anisotropy of its permittivity tensor ($\varepsilon_{11} \neq \varepsilon_{33}$).

We can define two refractive indices for the material: an *ordinary* one $n_o = \sqrt{\varepsilon_{11}/\varepsilon_0}$, for electromagnetic waves polarized perpendicular to the c axis, also called the crystal's *optical axis*, and a *extraordinary* one $n_e = \sqrt{\varepsilon_{33}/\varepsilon_0}$ for waves polarized in a direction parallel to it. Birefringence of the material is defined as the difference between such refractive indices $n_o - n_e$.

The material's refractive index dependence on wavelength in the UV-visible-IR range can be expressed in the Sellmeier equation form: [13]

$$n^2 = A_1 + \frac{A_2 + B_1 F}{\lambda^2 - (A_3 + B_2 F)^2} + B_3 F - A_4 \lambda^2 \tag{2.14}$$

where λ is expressed in µm and F is a temperature dependent parameter defined as:

$$F = (T - T_0)(T + T_0 + 546) \tag{2.15}$$

Table 2.5: Sellmeier equation coefficients for congruent lithium niobate, to be used in Equation 2.1.3. From [13]

	A_1	A_2	A_3	A_4
n_o	4.9048	0.117 75	0.218 02	0.027 153
n_e	4.5820	0.099 21	0.210 90	0.021 940

	B_1	B_2	B_3
n_o	2.2314×10^{-8}	-2.9671×10^{-8}	2.1429×10^{-8}
n_e	5.2716×10^{-8}	-4.9143×10^{-8}	2.2971×10^{-7}

with T expressed in °C and $T_0 = 24.5\,°C$. For congruent lithium niobate Sellmeier equation's coefficients are reported in Table 2.5, obtained in the 0.4-3 µm wavelength range. It should however be kept in mind that the Sellmeier equation depends on the crystal composition and may be affected either by the [Li]/[Nb] ratio, either by the presence of dopants.

ELECTRO-OPTIC EFFECT Lithium niobate is an electro-optic crystal as it shows a change in its refractive index if subject to an applied electric field. This behavior can be decomposed in both a linear and a quadratic response in the electric field **E**, respectively known as the *Pockel effect* effect and *Kerr effect*. Although lithium niobate shows a strong linear electro-optic effect, it has negligible quadratic electro-optic effect. [14]

The linear electro-optic response can be written in tensorial form as:

$$\Delta \left(\frac{1}{n}\right)_{ij} = \sum_k r_{ijk} E_k \tag{2.16}$$

where $\Delta \left(\frac{1}{n}\right)_{ij}$ is the second-rank tensor expressing the change in relative permittivity, E_k is the k component of the electric field, r_{ijk} is the third-rank linear electro-optic coefficient tensor and $i, j, k = x, y, z$. Applying properties and symmetries of the crystal makes it possible to write the 27 element linear electro-optic tensor as a 6×3 matrix of the following form, in which the components indices are written in Voigt notation:

$$r_{ijk} = \begin{bmatrix} 0 & -r_{22} & r_{13} \\ 0 & r_{22} & r_{13} \\ 0 & 0 & r_{33} \\ 0 & r_{42} & 0 \\ r_{42} & 0 & 0 \\ -r_{22} & 0 & 0 \end{bmatrix} \tag{2.17}$$

Table 2.6: Linear electro-optic coefficients $[\times 10^{-12}\,\mathrm{m\,V^{-1}}]$.

r_{42}	r_{22}	r_{13}	r_{33}	Ref.
28	3.4	8.6	30.8	[15]

PHOTO-REFRACTIVE EFFECT Another peculiar effect first discovered in lithium niobate by Ashkin et al. at Bell Laboratories is a variation of the crystal's refractive indices upon illumination. [16] This phenomena was initially known as *optical damage*, due to the fact that such an effect reduced the performance of devices based on such material as it resulted in unwanted decollimation and scattering of the beams passing through the material. This effect is actually a two step process, composed of a light-induced charge migration (due to BPVE for example) and a consequent linear electro-optical effect.

This property is strongly affect by defect and impurity densities in the material.

2.1.4 *Defects*

As briefly reported in the previous section, lithium niobate composition and defect densities can significantly alter the material's properties, especially photorefractive and photovoltaic ones. An overview of the defect types and their occurrence in lithium niobate will be provided in this section, both for *intrinsic* defects due to lithium niobate growth and composition and for *extrinsic* ones due to doping.

A crucial concept to understand the effect of such defects is the *polaron* one. A polaron is a quasiparticle originating from the coupling between an electron and the crystal lattice in which it moves. As the electron moves in the crystal, it interacts with it, locally altering the atomic displacements (phonons). This deformation in turns creates a potential well where the electron self-localizes. This quasiparticle has therefore a localized character, on the contrary to electrons in band states e. g. in metals or in semiconductors, which have a delocalized Bloch character.

Polarons are divided in *small* and *large* polarons based on the range of the electron-lattice interaction. In the small polaron case, the polaron radius is limited to a lattice site whereas large polarons radius can extend over several lattice sites. [17] Transport properties of small and large polarons are significantly different, with large polaron charge transfer being regarded as a band movement of a free-electron with an effective mass while small polaron transport is characterized by hopping from one site to the other. [7]

INTRINSIC DEFECTS Lithium niobate in the congruent composition has a [Li]/[Nb] ratio of 0.94 and thus has around 6% empty Li sites. This Li deficiency in cLN leads to the formation of a defects to compensate for the charge imbalance. Such defects are therefore regarded as of *intrinsic* type.

Several models can be developed to explain how such charge imbalance is compensated by the introduction of defects. The formation of oxygen vacancies (V_O[1]) is the most commonly occurring compensation mechanism for other oxides perovskites and in the $LiNbO_3$ case would be:

$$\langle LiNbO_3 \rangle \rightarrow Li_2O + 2V_{Li}^{-} + V_O^{2+} \tag{2.18}$$

Surprisingly, consistent experimental evidence, from structure to density measurements, hints to $LiNbO_3$ having almost no oxygen vacancies. The most striking evidence of this being the fact that a decrease in Li_2 is related with an increase in $LiNbO_3$ density, inconsistent with an oxygen vacancy model. [18]

This evidence suggests that some of the Li vacancies are filled with Nb atoms, forming *antisites defects*[2] Nb_{Li}. Two models have been proposed to account for this:

$$\langle LiNbO_3 \rangle \rightarrow 3Li_2O + 4V_{Li}^{-} + Nb_{Li}^{4+} \tag{2.19}$$

$$\langle LiNbO_3 \rangle \rightarrow 3Li_2O + 4V_{Nb}^{5+} + 5Nb_{Li}^{4+} \tag{2.20}$$

respectively called *Li site vacancy* and the *Nb site vacancy* models.

X-ray and neutron diffraction studies were able to measure that around 1% of the Li sites are occupied by Nb ions (Nb_{Li}), while around 4% of the Li sites are empty (V_{Li}), supporting the lithium vacancy model (Equation 2.20). [18] However some authors suggest all these cations stacking faults V_{Li}, V_{Nb} and Nb_{Li} coexists and their concentration largely depend on crystal growth conditions. [19]

EXTRINSIC DEFECTS Due to the high concentration of natural occurring vacancies, the doping of lithium niobate can be easily achieved during the growth process by direct melt doping or after through ion implantation.

Such doping introduces extrinsic defects which can significantly alter the material's properties, especially the photo-refractive and photovoltaic ones. Among the most common dopants for $LiNbO_3$ are Mg, Zr, Zn, Hf, In which increase the material's resistance to optical damage (reduce the photo-refractive effect), and Fe, Cu, Mn, Ni which

1 Common notation for defects A_B refers to a defect of type A located at the crystal lattice site of atom B.

2 Substitutional defects in a AB compound in which an atom of a certain type (A) replaces in its lattice position another atom of a different type (B).

instead are used to enhance the photogalvanic and photorefractive properties of the material. [7]

As for Fe and Cu impurities, a growing set of experimental evidence hints to their location at Li vacancies sites. [7, 20]

Iron impurity has been widely studied in $LiNbO_3$ and it exists in two charge states, Fe^{2+} and Fe^{3+} and has the effect of creating localized states in the band gap of the material. The Fe^{2+} impurities are responsible for the intense absorption band at 2.6 eV, with intensities linearly scaling with Fe^{2+} concentration, providing a method to quantify the impurity concentration from optical absorption measurements. [21, 22]

As will be clear in the next section, both intrinsic and extrinsic defects are crucial to the core mechanism of BPVE in Fe:$LiNbO_3$, which is the material studied in this thesis work.

2.2 BULK PHOTOVOLTAIC EFFECT IN LITHIUM NIOBATE

The main property we set to investigate in this thesis work is the *Bulk PhotoVoltaic Effect* (BPVE) a light-induced charge migration process with significant differences over other photovoltaic effects and typical of non-centro symmetric crystals such as lithium niobate.

The effect was first discovered by Glass et al. in 1974 which first measured a steady short-circuit current upon uniform illumination of Fe and Cu doped $LiNbO_3$ crystals. Such current was found to be proportional to light intensity and to the absorption coefficient and directed along the c axis only, with a negative charge carrier current flowing in the $+c$ direction. [5]

This phenomenon consists of a steady short-circuit current[3] in a solid under uniform illumination. The main difference with other photovoltaic effects consists in the fact that the charge migration is not due to an internal electric field, heterogeneity of the medium or a non-uniformity of the light field, but originates from the non-centro symmetric nature of the crystal, which under uniform illumination promotes charge migration in specific directions only. Due to the effect being displayed in uniform crystals under homogeneous illumination the effect was named *bulk* photovoltaic effect. [23]

Another striking difference from other photovoltaic effects is that the *photovoltage*[4] in BPVE can exceed the material's band gap by several order of magnitudes. For this reason the effect is also known as *anomalous* photovoltaic effect.

PHENOMENOLOGY The short-circuit current dependence on the electric field of the illuminating light can be modeled as the following tensor relation:

$$J_i = \sum_{jk} \beta^L_{ijk} e_j e_k I + i \sum_j \beta^C_{ij} [\mathbf{e} \times \mathbf{e}^*]_i I \tag{2.21}$$

where J_i is the current density vector, e_j and e_k are the unit vectors of light polarization, I is the light intensity and βijk is the photovoltaic tensor. The first term represents BPVE for linearly polarized light, while the second one expresses BPVE for circularly polarized light.

Considering the linearly polarized term only, the photovoltaic tensor β_{ijk} is a real third-rank tensor, with 27 elements. With symmetry arguments, the number of independent elements is reduced to 18, and

3 A current measured when the photovoltaic crystal is short-circuited and illuminated, due only to photo-generated charge carriers.

4 The voltage measured in the photovoltaic crystal in an open-circuit configuration, caused by illumination.

the tensor can be written as a 3×6 matrix and assumes the following form:

$$\beta_{ijk} = \begin{bmatrix} 0 & 0 & 0 & 0 & \beta_{15} & -2\beta_{22} \\ -\beta_{22} & \beta_{22} & 0 & \beta_{15} & 0 & 0 \\ \beta_{31} & \beta_{31} & \beta_{33} & 0 & 0 & 0 \end{bmatrix} \tag{2.22}$$

where Voigt notation was used for writing the tensor components indices.

Only four independent coefficients are needed to describe the photovoltaic tensor: [7]

$$\beta_{31} = \beta_{zxx} = \beta_{zyy} \tag{2.23}$$
$$\beta_{33} = \beta_{zzz} \tag{2.24}$$
$$\beta_{22} = \beta_{yyy} = -\beta_{xxy} = -\beta_{xyx} = -\beta_{yxx} \tag{2.25}$$
$$\beta_{15} = \beta_{xxz} = \beta_{yyz} \tag{2.26}$$

The magnitude of the photo-generated current in a specific direction can be expressed by the scalar expression, introduced by Glass in its original article [5]:

$$j_{phv} = k_G \alpha I \tag{2.27}$$

where α is the material's optical absorption coefficient, assumed to be isotropic, and $k_G = \beta_{ijk}/\alpha$ is the so-called Glass factor which characterizes the photovoltaic activity of a certain impurity in a particular crystal. This factor was found to be of the order of $10^{-9}\,\mathrm{A\,cm\,W^{-1}}$ for Fe:$LiNbO_3$. [5]

MICROSCOPIC INTERPRETATION A detailed microscopic interpretation of BPVE in Fe:$LiNbO_3$ was proposed by Schrimer et al., based on new experimental evidence acquired through pump-probe absorption studies using ultrafast fs pulses which evidenced the electron states involved in the process. [22]

The authors explain the effect as the result of a multi-step process involving the photo-induced release of electrons bound in polaron states and their subsequent hopping between impurity sites in the lattice, until such electrons are trapped back in deeper polaron states in impurities sites.

In Fe:$LiNbO_3$, Fe^{2+} impurities replace some of the Li^+ atoms, hence the notation Fe_{Li}, where the subscript indicates the atom the substitutional defect replaced. These Fe_{Li}^{2+} defects induce the appearance of energy levels in the $LiNbO_3$ bulk band gap. [24] Those levels are *polaron* states: bound states between an electron and a lattice phonon (subsection 2.1.4).

Such Fe_{Li} impurities are responsible for the intense absorption band in Fe:$LiNbO_3$ with an onset around 1.6 eV and maximum around 2.6 eV.

[22] The optical absorption of Fe_{Li} defects can be interpreted as a light-induced transition of a small polaron bound to a Fe^{3+}_{Li} to one of the eight neighboring Nb^{5+}_{Nb} sites.

The transition probability from the Fe^{2+}_{Li} site to one of the eight Nb^{5+}_{Nb} is not the same since the eight Nb atoms are located on non-equivalent sites and decreases with distance. The authors were able to explain the $+c$ direction of the photovoltaic current as originating from such differences in the transition probabilities to Nb^{5+}_{Nb} sites. In a similar way also other substitutional defects in Li sites, such as Nb_{Li} antisite defects, cause similar light-induced charge transfer.

This light induced transition makes it possible for electrons to move in a band-like, coherent motion in the crystal. The newly emitted *"hot" electron* is initially delocalized and has a wave-like character, but soon loses its energy by phonon scattering, until it reaches the bottom of the conduction band. Its motion is then terminated by the formation of a Nb^{4+}_{Nb} small free polaron. The coherent part of this charge transport along the c axis can be expressed in terms of a mean transport length $\Lambda^{coh}_z(\hbar\omega)$:

$$\Lambda^{coh}_z(\hbar\omega) = \frac{\sum_{1,2,3,7} p_i(\hbar\omega) l^{coh}_{i,z} - \sum_{4,5,6,8} p_i(\hbar\omega) l^{coh}_{i,z}}{\sum_{i=1,\dots,8} p_i(\hbar\omega)} \tag{2.28}$$

where p_i are transition probabilities for electrons from the Fe^{2+}_{Li} site to the i-th Nb^{5+}_{Nb} one and $l^{coh}_{i,z}$ is the projected transport length along c. We can express such current in the scalar expression, modeled after Equation 2.27

$$j_{phv} = e\dot{n}_e \Lambda^{coh}_z(\hbar\omega) = e\left(\frac{\alpha I \Phi}{\hbar\omega}\right)\Lambda^{coh}_z(\hbar\omega) \tag{2.29}$$

where $\dot{n}_e$ is the *optical production rate* and Φ is the quantum efficiency expressing the number of excited electrons per absorbed photon.

These Nb^{4+}_{Nb} polarons take part in a thermal activated hopping between several Nb_{Nb} sites, which represents an incoherent diffusive transport. Such polarons are then trapped in deeper defects such as the Nb^{5+}_{Li} and Fe^{3+}_{Li} impurities, which lead to the formation of the same states from which the process originally started with the optical absorption, ending the charge transport.

It appears that the coherent part of the polaron transport is the reason for the establishment of the photovoltaic current in the c direction, while the incoherent part, associated with a low mobility, is the reason for the limited recombination to the original impurity sites, and explains how high open-circuit fields (up to $E_{ph} = 10^5\,\mathrm{V\,cm^{-1}}$) are possible in BPVE in the material.

The measured open-circuit field is given by the expression:

$$\mathbf{E_{phv}} = \frac{\mathbf{j_{phv}}}{\sigma_I + \sigma_D} \tag{2.30}$$

where σ_D is the *dark* conductivity of the crystal, that is conductivity for the material in absence of illumination, and σ_I is the crystal's *photo-conductivity*, which can be expressed as:

$$\sigma_I = e\dot{n}_e \mu\tau \tag{2.31}$$

where μ is the charge carrier mobility and τ is the carrier lifetime.

Using Equation 2.29 and Equation 2.30, an experimental value of $E_{phv} = 10^5\,\mathrm{V\,cm^{-1}}$ and theoretical estimates of 1 Å Λ_z^{coh} it was possible to estimate the product $\mu\tau = 10^{-13}\,\mathrm{cm^2\,V^{-1}}$. [22]

A significant increase in the extracted photocurrent it is expected for a thin film with thickness of the order of the thermalization length, due to ballistic charge transport.

From *ab initio* simulations of the system, thermalization length is predicted to be around the nm in the optical and UV frequency range. [25][5]

5 In the reference, the λ_t values for 520-560, 580 and 600 nm were misprinted and must be multiplied for 10^1 to obtain the correct value.

3

SYNTHESIS OF LITHIUM NIOBATE THIN FILMS

To study the effect of BPVE in systems at the nanoscale, we decided to synthesize Fe:$LiNbO_3$ thin films, adopting a bottom up approach. The ideal system to perform our experiment is a heterostructure composed of a crystalline thin film enclosed between two electrodes. We decided to deposit the film on a conductive substrate, which provides a back electrode for photoconductivity measurements. Since a high-quality crystalline film is required, we chose to use a conductive substrate that could work as epitaxial template as well. A transparent contact would be deposited on the surface of the film as the front electrode.

In this chapter information will be provided regarding the technique used and the choices we made for the synthesis of Fe:$LiNbO_3$ thin films analyzed in this thesis.

3.1 LITHIUM NIOBATE THIN FILMS

The ability to synthesize high-quality lithium niobate thin films on commonly available substrates would open many other possibilities with integration in electronic circuits and integrated optical devices.

As such properties are highly dependent on the material composition and its impurities, it is crucial to evaluate the quality of the produced thin films and study how it is affected by the specific growth techniques used.

SYNTHESIS TECHNIQUES Several methods have been historically used to synthesize $LiNbO_3$ films such as Pulsed Lased Depostion (PLD), Liquid Phase Epitaxy (LPE), Chemical Vapor Deposition (CVD) and Radio-Frequency Magnetron Sputtering (RFMS). Each of them has its advantages and carries limitations and drawbacks. As an example of this, Pulsed Laser Deposition can preserve the elemental composition of the source but, due to the limited area of illumination by the laser, results in the production of inhomogeneous samples. [26]

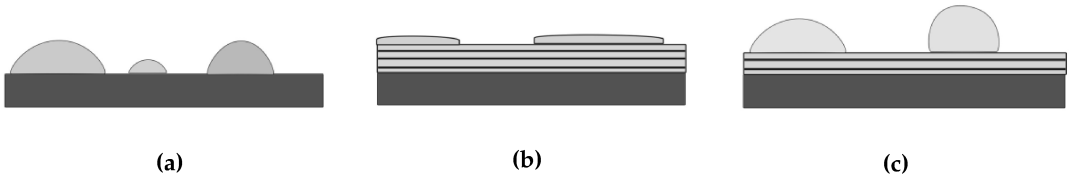

(a) (b) (c)

Figure 3.1: Schematic representation of the three epitaxial growth models. From [27]

One of the most promising methods is Radio Frequency Magnetron Sputtering, which consists in erosion of a target with a plasma and the deposition of the ablated material on the substrate. This technique allows to deposit homogeneous films using a wide range of materials, independently of their melting temperature. Thickness of the films can be easily controlled and the process can be used to deposit films on a large area and with an high deposition rate. The main difficulty of this technique arises from the use of a plasma, which requires a detailed characterization and calibration of the deposition process as a function of the operating parameters For all these reasons we chose this technique for the deposition of our samples. The working details of the technique will be explained in detail in section 3.2.

GROWTH MECHANISMS The growth process of the film starts with deposition of atoms on the substrate and their diffusion on its surface. Atoms can combine and form clusters (nucleation), which are the starting point of the epitaxial film growth. Film growth in sputtering can take place by different regimes, dependent on the substrate and deposition conditions, and the most common ones are described by three basic models.

The first model is the *Volmer-Weber model* (Figure 3.1a), which describes growth in the case of poor adhesion between the crystallites and the surface. In this model, the diffusing atoms form clusters and growth takes place around such islands, which can eventually coalesce and form a continuous film. Another model is *Frank-van der Merwe model* (Figure 3.1b), in which the high adhesion of the atoms to the substrate leads to film growth layer by layer. An intermediate growth regime between the first two is represented by *Stranski-Krastanov model* (Figure 3.1c) in which the film grows in layers for several monolayers up to a thickness at which it starts to grow by nucleation and coalescence of the clusters.

The assumed growth mechanism for $LiNbO_3$ thin films grown by the deposition techniques previously reported is Volmer-Weber model, in agreement with previous studies. [27, 28]

SPUTTERING PARAMETERS To ensure high quality film growth, the sputtering process parameters and their effect on the growth process must be studied in detail. The most important parameters in RFMS are the composition of the target, the substrate-target distance, the substrate type and its temperature, the atmosphere composition and the total pressure inside the deposition chamber.

As for the target composition, both single crystals and sintered targets have been studied, with single crystals appearing to be more favorable targets for the formation of highly crystalline films, with elemental composition matching the target one.

RF power appears to strongly affect the degree of crystallinity of the film, with most authors reporting amorphous growth for values below 70 W, due to the insufficient energy of the sputtered species to perform nucleation on the surface. It is reported that for RF power values of 100 W crystalline films are obtained and surface roughness is minimized in the deposited films (Figure 3.2a). Higher values of RF power can lead to heating of the target, leading to the dissociation of oxygen and lithium, which result in the films growing in Li poor phases. [27]

The type of substrate will directly affect the growth rate, structure and composition of the lithium niobate thin film, as the crystalline structure of the substrate will affect the thin film one. As for the temperature of the substrate during deposition, it is reported that amorphous films are formed for non-heated substrates and that a temperature of 560 °C is optimal for oriented growth of crystalline films. Temperature higher than 600 °C can cause evaporation of lithium from the surface of the film, leading to lithium poor phases.

The most critical parameters for RFMS appear to be the working gas pressures and compositions, as they influence the properties of the plasma, growth rate and roughness of the films. High working pressures ($(1.3-2.6)10^{-2}$ mbar, 10−20 mTorr) tend to produce to films having a low lithium concentration and growing lithium deficient phases. This can be explained as at higher pressure lithium ions' mean free path in the plasma is reduced, due to the ion's low atomic mass which increases its scattering in the plasma, thus reducing the number of ions reaching the surface and taking part in the expitaxial growth.

This effect also explains the decrease in the deposition rate shown in Figure 3.2b for pressures higher than 10 mTorr. [30] It is reported that lower working gas pressures, around $(1.3-2.6)10^{-3}$ mbar (1-2 mTorr), result in films having a high degree of crystallinity at the expense of slower deposition rates.

Another critical parameter is the atmosphere's composition in the deposition chamber, which especially affects the lithium concentration in the films. Lithium niobate films often grow with a lithium deficiency

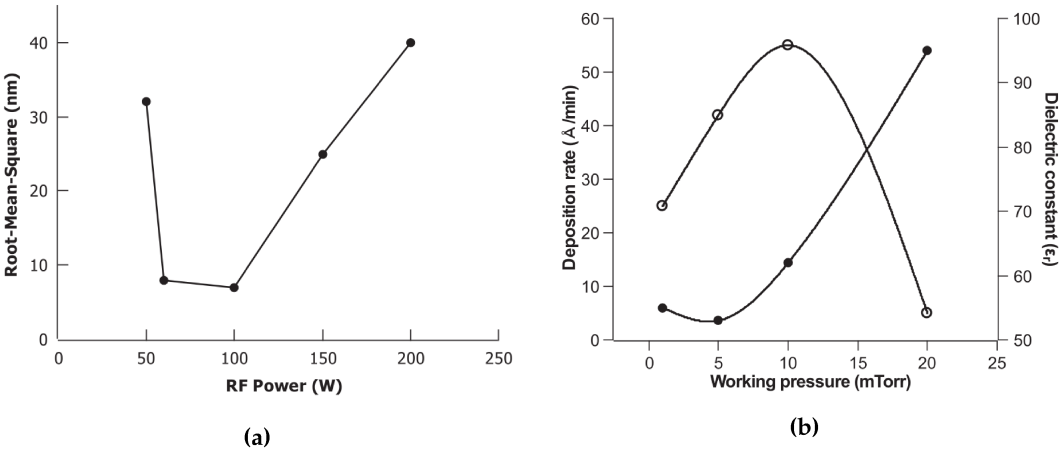

Figure 3.2: Dependence of film parameters on RF power **(a)** and working pressure **(b)**. RMS roughness is reported in **(a)** as a function of RF power. Deposition rate in **(b)** is shown in white circles. Respectively from [29] and [30].

using RFMS and other methods. Using O_2 in the deposition chamber can increase lithium's partial pressure. [31] However, the use of pure oxygen atmosphere results in fabrication of multi-phase $LiNbO_3$ thin films. [32] For this reason, an Ar/O_2 mixture is often used, with ratio varying from 1:1 up to 5:1. The effect of the ratio choice is to be evaluated together with other deposition parameters, as they jointly affect plasma properties.

The oxygen concentration, the total pressure and the target-substrate distance affect the kinetic energy of the sputtered atoms and must be optimized to obtain the desired epitaxial growth. If the sputtered atoms have high energy, as in a low oxygen atmosphere, the films grow with many defects while if their energy is too low, for example as the result of a high number of collisions with oxygen atoms, films grow with a reduced degree of crystallinity. The most common value for the sputtering target-sample distance in literature is 5 cm, and this must be taken into account when evaluating a certain set of the other operating conditions.

In some cases, if the deposited films show low degree of crystallinity, thermal annealing can be performed after the deposition, to further improve crystal quality. Such process is usually performed either in air or in an oxygen atmosphere, this latter choice intended to reduce lithium evaporation at high temperatures.

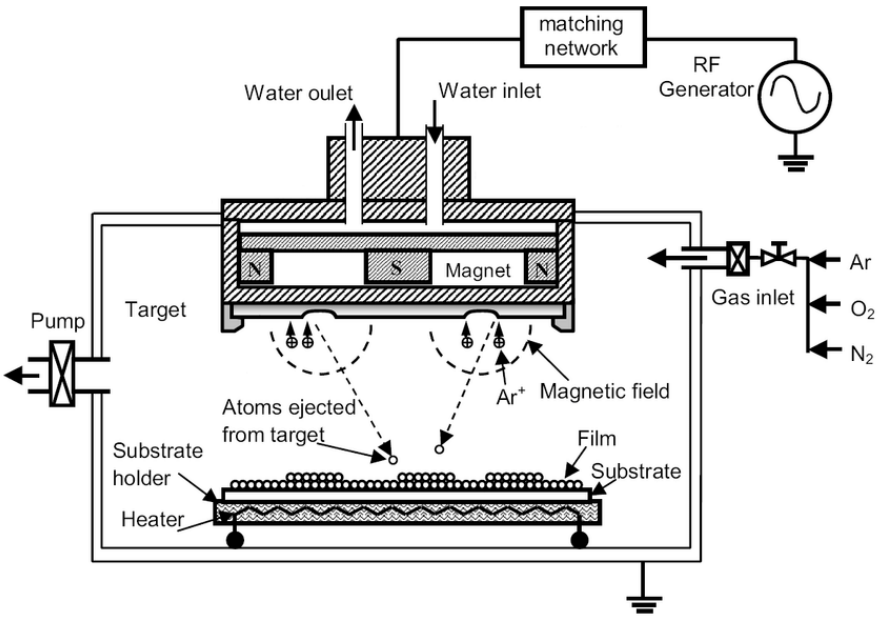

Figure 3.3: Schematic drawing of a RFMS apparatus. From [33]

3.2 SPUTTERING PROCESS FOR THIN FILMS DEPOSITION

The technique used for the deposition of our samples is *Radio Frequency Magnetron Sputtering*, a versatile physical deposition technique which allows to create uniform thin films of controlled thickness.

In sputtering deposition techniques a flow of atoms and clusters is obtained by ion bombardment of a *target* material. Energetic ions, often in a plasma, impact on the target surface, transferring their momentum to atoms on the surface and causing their release from the material. The sputtered atoms or clusters ballistically propagate in the deposition chamber and deposit onto the desired substrate,

A schematic of a RFMS sputtering apparatus is shown in Figure 3.3. A sputtering apparatus is enclosed in a vacuum chamber to ease the formation of a plasma by control of the gas pressure and avoid contamination during the deposition process. Before the deposition, the chamber is brought to high vacuum levels (10^{-6} mbar) and then filled with inert gas (such as Ar) to pressures of the order of 10^{-4} mbar. The sputtering system is mainly composed of a target and a substrate, which are respectively located over a planar cathode and anode, connected in a high voltage circuit.

A high potential difference is established between the two electrodes to cause electrons to be emitted from the cathode and to ionize some of the inert gas atoms, forming a plasma. The gas ions are then accelerated by the electric field towards the anode and impact on the target surface, causing the release of atoms from its surface. This basic system is what is generally known as DC sputtering apparatus.

More efficient variants of this setup were developed to improve the generation of a plasma from the inert gas. Such variants are the magnetron and RF sputtering setups.

In magnetron discharge, the target is located on top of a set of permanent magnets, forming a magnetic field which, combined with the electric field between the two electrodes, results in the electrons from the plasma being confined in the target region, increasing the ionization probability. This is obtained by choosing magnetic field strengths which are able to confine electrons close to the target. Ions, on the other hand are only weakly affected by the field, due to their larger mass. [27] These improvements make it possible to reduce the inert gas pressure inside the chamber, reducing diffusion of the sputtered particles and thus enabling proper ballistic motion towards the substrate.

In insulating materials, the sputtering process can lead to a positive charge buildup on the surface of the target, which alters the plasma dynamics and can stop the sputtering process. To avoid this RF sputtering was developed, a technique in which the DC voltage is replaced by a Radio Frequency alternating voltage, usually at 13.56 MHz. The alternating voltage makes it possible for the target to discharge during each cycle, solving this issue and also reducing the risk of electric arc discharge appearing in the plasma.

In an RFMS setup these two modifications are combined and allow an efficient and stable sputtering operation at low gas pressures.

Thanks to the stable operation, films of different thickness can be repeatably obtained by varying the duration of the sputtering run.

The RFMS sputtering equipment used in this thesis is located at Molecular Science and Nanosystems Department of Ca' Foscari University of Venice. In this apparatus the sample holder could be heated at high temperatures, up to 450 °C, to improve the crystal quality of the deposited film.

3.3 CHOICE OF THE SUBSTRATE

As the bulk photogalvanic effect is strictly dependent on crystalline structure and specific crystal directions, it is necessary to look for an appropriate substrate, promoting epitaxial growth of a crystalline film in the directions of interest.

As we're interested in measuring photocurrents in a thin film heterostructure, with electrodes located on top and on the substrate, the Fe:$LiNbO_3$ film had to grow in the $(0\,0\,1)$ orientation, with the c axis, which is parallel to the direction of the photocurrent (see Equation 2.2), perpendicular to the surface of the sample.

In the search for a substrate matching the $(0\,0\,1)$ $LiNbO_3$ face other constraints were imposed. As we wanted to employ the substrate as a back contact in our heterostructure, we looked for electrically conductive substrate materials. Additionally we wanted the substrate to be transparent to visible light in order to avoid other absorption mechanisms in the substrate to alter the thin film behavior and to be able to perform optical absorption spectroscopy on the thin films.

Our final choice for the substrate material was gallium nitride (GaN), a transparent wide gap semiconductor intensively researched in the last two decades for its applications in opto-electronic devices in the green, blue and ultraviolet range and in high-power and high-temperature applications. GaN can be doped either in p- or n- character, therefore satisfying our requirement for a conductive substrate.

GaN typically grows in wurtzite crystal structure, with lattice parameters of a $a = 3.189\,\text{Å}$, $c = 5.185\,\text{Å}$. Epitaxial growth of c-axis oriented $LiNbO_3$ films on $(0\,0\,1)$ GaN is reported in literature. [34] Both crystals show an hexagonal structure on the $(0\,0\,1)$ side and, with a relative in-plane rotation of 30° show a lattice mismatch of 6.8% relative to the GaN lattice parameter. [34, 35] The relative orientation of the GaN and $LiNbO_3$ $(0\,0\,1)$ faces is shown in Figure 3.4. The 30° in-plane rotation between the two hexagonal lattices can result in the crystal growing in grains having relative orientation of 60° between each other.

Ever since GaN has found a groundbreaking commercial application in LED production, GaN wafers can be easily acquired in various specifications. Our choice was for 5 µm GaN films on 430 µm sapphire wafers. The wafers were bought with different doping type: a Mg doped one, showing positive charge donor character and a Si doped one, having n-type character. This choice was made to allow the study in future works of the effect of the substrate charge carriers on BPVE current extraction.

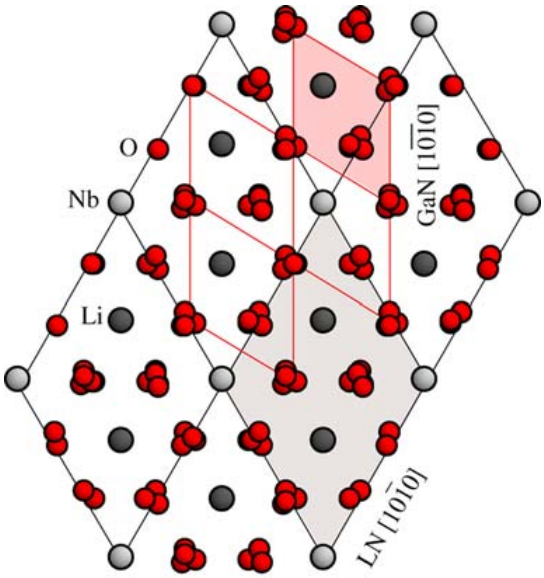

Figure 3.4: Relative orientation of $LiNbO_3$ and GaN hexagonal unit cells in epitaxial growth of GaN on $LiNbO_3$. From [35].

3.4 CHOICE OF SPUTTERING PARAMETERS

As explained in Figure 3.1 several parameters influence the outcome of $LiNbO_3$ sputtering depositions.

First and foremost, the choice of the target used for sputtering is crucial in the determination of the film composition. We chose to follow the general advice found in literature and used a single crystal $LiNbO_3$ target, a choice which is reported to ensure a good degree of crystallinity and preservation of the original elemental composition. [27] In order to introduce Fe doping in our films, a commercially available Fe:$LiNbO_3$ crystal was first used. However, this crystal was too thin and shattered during the first use, leading to sample contamination. For this reason a single crystal $LiNbO_3$ target was then used, adding small pieces of iron on its surface, covering an area of around 1% of its surface.

Once the substrate and the target have been chosen, the most significant parameters left to be configured are RF power, target-substrate distance, substrate temperature and the pressure and ratio of the gases in the deposition chamber. The interplay between these few parameters can lead to very different outcomes of the sputtering process, and for this reason they must be tuned in several configurations.

The target was fixed at a 5 cm distance from the substrate, as referenced in most of the literature on the topic. The substrate temperature was set at 450 °C to aid the crystallization process during epitaxial growth.

With these two parameters fixed, we proceeded to combine the remaining variables in three experimental configurations used for the three sputtering runs.

We chose to use RF power of 100 W for all three runs, a value recommended for the type of oriented crystalline growth of our interest, and reduce the pool of parameters to be explored. We decided to perform two runs at 40×10^{-4} mbar total pressure, at Ar:O_2 ratios of 2:1 and 7:2, and one run at 15×10^{-4} mbar total pressure, with a Ar:O_2 ratio of 2:1.

3.5 SAMPLE PREPARATION

In this section, the multi-step process for the sample synthesis will be explained.

The first step in the production of our samples is cutting the substrate for deposition. The substrate of choice for the samples produced during this thesis work are commercial GaN on sapphire wafers of 2 inches of diameter. The GaN film has a thickness of 5 µm over a 430 µm sapphire substrate.

Two types of substrates were used, p- and n-doped GaN substrates, in order to test the effect of the substrate on the film electrical properties. The p-doped substrate was doped with Mg and was polished only on the GaN side, while the n-doped one was Si doped and polished on both sides.

This choice of transparent substrates and in particular of the double polishing of the n-doped ones was made to make it possible to perform UV-Vis absorption spectroscopy on the film, in order to measure absorption properties and other characteristics of the film.

To distinguish between the two sides of the wafer, electrical conductivity measurements on each side were performed, using a multimeter. The sapphire side showed a very high resistivity, over the highest measurable value for the multimeter, while the doped GaN side had a high but measurable resistivity, in the order of the MΩ.

The substrate wafers were cut in samples of 10x12 mm using a diamond dicing machine, with the long side parallel to the GaN $(0\,1\,0)$ crystal direction.

Once the samples were cut we proceeded to carefully clean them, in a four steps routine intended to remove every contaminant on the surface which could alter the growth of the film such. This cleaning procedure is a standard procedure for hard materials which need to be polished without any scratching. Samples were first cleaned with a solution of soap in distilled water, then washed with acetone, later in ethanol and lastly with isopropyl alcohol. Each solution used in

Table 3.1: Sputtering deposition parameters for the samples analyzed in this thesis. Target distance is denoted with d, RF power with P_{RF}, sputtering duration with t.

Sample	P_{tot} (10^{-4} mbar)	P_{Ar} (10^{-4} mbar)	P_{O_2} (10^{-4} mbar)
N1, P1	40	26	14
N2, P2	41	32	9
N3, P3	15	10	5
Sample	P_{RF} (W)	d (cm)	t (s)
N1, P1	100	5	1800
N2, P2	100	5	1800
N3, P3	100	5	1800

the cleaning process is used to remove traces left from the previous one. To avoid scratching, the samples were cleaned in each step by performing an ultrasonic bath while immersed in each of the four solutions. Between each step, the samples were dried using clean compressed air.

After cleaning, the substrates were ready for film synthesis by RF magnetron sputtering. Three deposition runs were performed using different combinations of sputtering parameters. In each deposition run sputtering was performed on two samples at a time, one on a p- and one a n-doped substrate, in order to obtain samples differing only on the substrate doping. On each sample, part of the substrate was masked to preserve an access point to the GaN substrate for the placement of contacts for future electrical measurements.

To aid in the formation of a crystalline thin film, the substrate was heated during deposition at a temperature of 450 °C.

Table 3.1 contains the summary of the sputtering parameters used in the three runs.

All the three sputtering runs were successful and resulted in the deposition of Fe:$LiNbO_3$ films. The obtained samples were transparent and appeared free of noticeable defects.

In the next chapter characterization of such samples will be reported in detail.

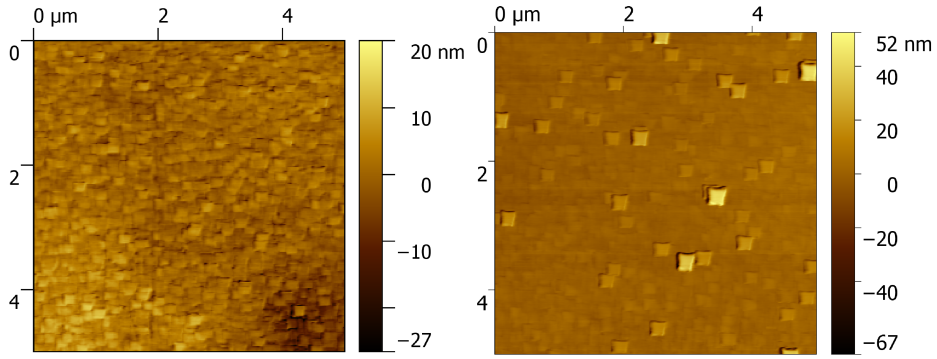

(a) N1 **(b)** N2

Figure 3.5: AFM maps of the sample's surface, for samples N1 and N2. Data from [25]

3.6 SAMPLE TOPOGRAPHY CHARACTERIZATION

The first characterization for our samples consisted in a quick topographic survey of the films and a profilometric measurement of their thickness, performed after a cleaning routine on the samples.

In order to obtain a first measure of the film thickness, a contact profilometer was used. Such instrument is composed of a diamond stylus which is brought to contact with the surface and moved across the sample surface while recording its vertical displacement. This way, surface profile lines can be obtained over lengths of several hundred µm.

To obtain the film thickness, we measured the step height between the film an uncovered part of the GaN substrate, at the border of an area in which the film was not deposited. As earlier stated, before deposition we proceeded to mask part of the substrate using small pieces of a Si crystal, in order to keep an access point to the substrate for electrical measurements. This resulted in the formation of a sharp edge between the deposited film and the substrate in those regions, which made it possible to measure the film thickness.

Several line scans were performed at the edge of this region and the resulting step heights were averaged to compute an estimate of the thickness. Its uncertainty was estimated as the difference between the maximum and minimum measured step heights, to give information about the range of variations in the edge region. We must keep in mind that this is a local estimate and surface averaged measurements such as from optical absorption or XRR would be preferred. The obtained film thicknesses are reported in Table 3.2. We measured also some additional samples that will be used in the next sections as reference. Those samples consist of a Substrate(LN)/SiO_2/Pt/Cr/Fe:LN heterostructure produced by Smart Cut (also known as ion slicing)

Table 3.2: Thickness determination for various samples analyzed in this thesis.

Sample	d (nm)	Source
P1	200(30)	profilometer
N1	200(20)	profilometer
P2	300(20)	profilometer
N2	270(20)	profilometer
P3	210(30)	profilometer
N3	170(20)	profilometer
Fe:$LiNbO_3$ SC	295(2)	manufacturer
Fe:$LiNbO_3$ SC	295(2)	manufacturer
cLN SC	717.0(4)	manufacturer

Table 3.3: AFM measured RMS roughness for samples analyzed in this thesis.

Sample	z_{RMS} (nm)
P1	1.57(1)
N1	1.68(1)
P2	5.6(1)
N2	4.7(1)
P3	0.418(1)
N3	0.804(1)

technique by the NanoLN company. The Fe:$LiNbO_3$ layer thickness for these samples was manufacturer provided one.

AFM scans were performed on different parts of the samples to inspect the surface for unusual features and to estimate the surface roughness. This quantity was locally estimated on 5x5 µm areas as a RMS roughness. The obtained values for this parameter are reported in Table 3.3, while some AFM maps of interest are reported in Figure 3.5.

The maps for samples deposited in run 3 were omitted as they showed a smooth surface and no apparent features. The other samples had surfaces with roughness of the order of a few nm.

In the AFM maps for samples N1 and N2 we can notice rectangular features, of 150-200 nm long sides, and height varying from a few nm up to 80 nm.

As it can be clearly noticed, the samples show different surface morphology, as a result of different deposition conditions. The squared features hint to crystalline growth of the film and are probably growth facets. However their rectangle-like appearance cannot be explained with respect to the three-fold rotation symmetry of the $LiNbO_3$/GaN interface and further investigation on this aspect is being carried out.

We can notice an increase in their height from the first to the second deposition (20 to 80 nm), which, along with an increase in thickness signals a faster growth rate. As the only different parameter in these runs was the Ar:O_2 ratio, this different growth rate could be correlated with a different crystal composition. Compositional analysis will allow us to measure differences in their composition.

Samples produced in the third run have thickness comparable to the run 1 samples, but completely different surface morphology. They show a smooth surface without regular surface features. This characteristic could probably be explained considering a re-sputtering phenomenon. Since in this run the chamber pressure was kept at a lower level compared to the previous ones, the energy distribution of the ions inside the chamber is peaked at higher values, because of the reduced number of scattering events. As consequence a number of energetic ions impinge on the sample during the deposition and may eventually erode the deposited film, removing the presence of topographical features.

4

THIN-FILM CHARACTERIZATION TECHNIQUES

The characterization of the epitaxially grown thin-films involves using a wide array of techniques, to obtain compositional, structural information on the film and on its response to external electric fields.

The techniques used are optical transmission spectroscopy (UV-Vis) for film thickness, High-Resolution X-Ray Diffractometry (HR-XRD) for crystalline structure analysis, Rutherford Backscattering Spectrometry (RBS) and Nuclear Reaction Analysis (NRA) for compositional analysis.

4.1 HIGH-RESOLUTION X-RAY DIFFRACTOMETRY

In the context of characterization of crystalline thin films, techniques based on X-ray diffraction (XRD) and reflection (XRR) hold a fundamental role, as such measurements are able to provide countless information on structural film properties and on many types of crystal defects. These techniques are largely used in semiconductor research, due to the high precision of such measurements and the ability to easily probe multi-layered thin film systems.

In this thesis, mostly High-Resolution X-Ray Diffractometry (HR-XRD) was used, employing the *Reciprocal Space Map* (RSM) method.

4.1.1 *Introduction*

In this type of analysis the crystal structure is probed by sending x-ray radiation, which has wavelength of the order of the crystal interplanar spacing, and measuring the intensity of the x-ray radiation diffracted by the crystal as a function of the angles between the source, the crystal and the detector. Diffraction from crystal structures is an elastic scattering process, which involves the interaction of the x-ray radiation with the atomic electron cloud. Being an elastic scattering process, the incident photon energy (or wavelength) is not modified

by the scattering and the radiation is re-emitted only with a change in its propagation direction.

In HR-XRD the incident radiation is highly collimated, so that it can be well approximated by a plane wave with a single wave vector $\mathbf{K_0}$, and the x-ray intensity is measured using a highly-resolved angular detector system, so that the measured intensity can be attributed to a well defined plane wave with $\mathbf{K_h}$ wave vector. In such experiments we measure the x-ray intensity as a function of the *scattering vector*:

$$\mathbf{S} = \mathbf{K_h} - \mathbf{K_0} \tag{4.1}$$

As the scattering is elastic, $|\mathbf{K_h}| = |\mathbf{K_0}|$, the scattering vector's length and direction are determined uniquely by the angle between the incident and outgoing radiation wavevectors.

Von Laue's picture of x-ray diffraction as the result of scattering from a set of individual scattering sources which form a periodic structure (Bravais lattice), results in a simple constructive interference condition. Diffraction maxima are found when the difference between the incoming and reflected wavevectors, $\mathbf{S}$, is equal to a crystal's reciprocal-space vector $\mathbf{G}$, which can be related to specific interplanar distances in the crystal. When this happens, the constructive interference condition holds for every set of scatterers displaced from one another by a real-space Bravais lattice vector $\mathbf{R}$: [36]

$$\mathbf{R} \cdot (\mathbf{K_h} - \mathbf{K_0}) = \mathbf{R} \cdot \mathbf{G} = 2\pi m \tag{4.2}$$

with m an integer number.

A graphical construction known as *Ewald construction* makes it easy to apply Von Laue condition for x-ray diffraction. A sphere can be built in reciprocal space having the incident wavevector $\mathbf{K_0}$ as its radius. Due to the elastic scattering constraint, the diffracted wavevector must have the same length as the incident one. By placing the end of an identical vector, parallel to the diffracted wavevector, at the tip of the incident one, the sum of the two vectors is a vector between two point on the sphere, the scattering vector $\mathbf{S}$. If these two points are reciprocal *lattice* points, Von Laue condition for diffraction is true and that reflection will be measured in that $\mathbf{K_0}$, $\mathbf{K_h}$ configuration.

By changing the angles between the crystal and the incident and diffracted beams, we're able to control the scattering vector's length and direction and effectively probe the crystal's reciprocal lattice by measuring the various diffraction peaks, also called *Bragg's reflections*, related to scattering by different crystal plane families.

The scattering vector can be controlled by setting different values for the two principal angles in the setup: the ω and θ angles. Those two are the angles between the incident radiation wave vector and a plane:

the sample surface for ω or a crystal plane when the sample is close to Bragg's condition in the case of θ. The angle between the incident and diffracted radiation wave vectors equals 2θ. The ω and θ angles can differ in the case the selected crystal plane is not parallel to the sample surface. In our experimental apparatus, the ω angle and the 2θ angles are measured by means of two high precision goniometers setting the direction of the incident beam with respect to the sample surface and the direction of the diffracted beam with respect to the primary one, respectively.

By changing the θ angle, it's possible to modify the length of the scattering vector $\mathbf{S}$, while its direction can be tuned by operating on the ω angle. Therefore one can investigate different parts of the crystal's reciprocal space by altering the crystal orientation with respect to the x-ray beam and by tuning the scattering vector length, all by changing the ω and θ angles respectively.

A schematic depiction of a reciprocal space scan is reported in Figure 4.2 for a GaN crystal. In this figure is shown the reflection of an incident plane wave of $\mathbf{K_0}$ wave vector and θ incident angle on a crystal plane. The outgoing wave vector $\mathbf{K_h}$ and the scattering vector $\mathbf{S}$ are shown. The $\mathbf{S}$ vector points to a reciprocal space point, corresponding to a specific reflection. Other possible reflections are shown. By changing the angle of diffraction θ, the length of the scattering vector can be modified. By introducing a tilt of the sample, an ω offset can be introduced, modifying the scattering vector direction with respect to the sample normal.

Angular coordinates can be converted to reciprocal lattice coordinates using the following expressions: [37]

$$S_{\parallel} = \frac{2\pi}{\lambda}\left(\cos(\omega) - \cos(2\theta - \omega)\right) \tag{4.3}$$

$$S_{\perp} = \frac{2\pi}{\lambda}\left(\sin(\omega) + \sin(2\theta - \omega)\right) \tag{4.4}$$

where S_z is the coordinate relative to the direction parallel to the sample surface normal and S_x is the coordinate parallel to the in-plane component of $\mathbf{K_0}$. S_x and S_z define the scattering plane, in reciprocal space.

Not all of the reciprocal space can be probed in a setup with fixed x-ray wavelength and a certain maximum θ. The outer semi-circle has a radius twice the incident wave vector and represents the maximum length of the scattering vector, at fixed λ and maximum θ. By changing ω to tilt the crystal, it's possible to move such vector. However, the gray shaded area shows a reciprocal space region which cannot experimentally be probed, as such tilt of the sample would either block the incident or outgoing beams. [37]

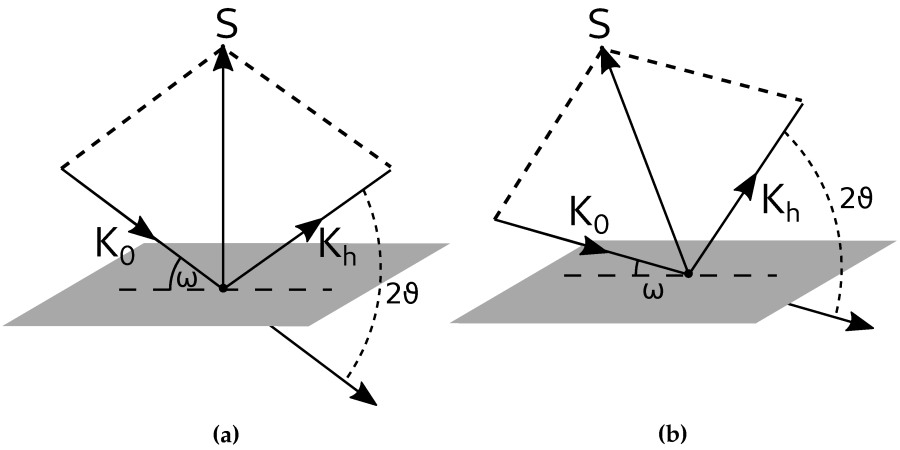

Figure 4.1: Diagrams for symmetric ($2\omega = 2\theta$, **(a)**) and asymmetric ($2\omega \neq 2\theta$, **(b)**) diffraction geometries. In the asymmetric ones an offset is introduced to tilt the scattering vector **S**.

Reciprocal Space Maps are usually obtained by taking $\omega - 2\theta$ scans at different ω sample tilt. In the $\omega - 2\theta$ scans the sample is rotated by $\Delta\omega$ and the detector is rotated by $\Delta 2\theta$, so that the angular ratio between such changes is kept 1:2. In reciprocal space this results in the increase of the scattering vector length, without any change in direction, which is instead modified by the ω offset which is changed from scan to scan (Figure 4.1).

The position of the reflections and their broadening can provide a wealth of information, which is especially easy to access in RSM.

4.1.2 *Experimental details*

In our experiments a Philips Analytical[1] X'Pert PRO Materials Research Diffractometer (MRD) was used.

In this apparatus, the x-ray radiation was produced by a copper-anode tube, operated at 40 mA and 40 kV, which results in a Cu $K_{\alpha II}$ x-ray emission at $\lambda = 1.540\,56$ Å.

The incident beam was directed to a four-bounce Bartels Ge $(2\,2\,0)$ monochromator [38] and a parabolic multilayer mirror, which were able to produce a highly monochromatic beam with a divergence of $0.0034°$ in the equatorial plane and spectral purity of $\Delta\lambda/\lambda = 10^{-5}$.

The sample is mounted on a Eulerian cradle with a motorized sample stage which allows its rotation along two axes and small translations of the sample along three Cartesian axes allowing to set the desired crystal planes in diffraction condition or move along the sample. Both the sample and the detector are mounted on two co-axial high precision goniometers (accuracy of $0.0005°$) which control the ω and

1 Now Malvern Panalytical

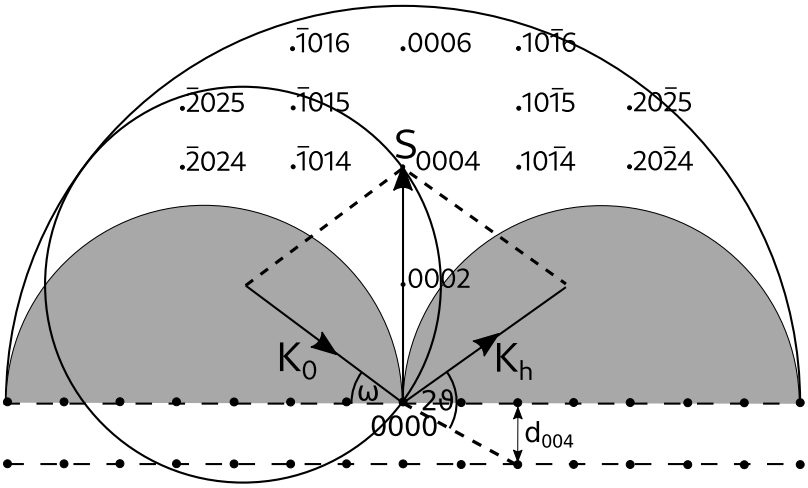

Figure 4.2: Reciprocal space section schematic for a $[0\,0\,0\,1]$-oriented GaN film. Regions of reciprocal space where the sample blocks a beam are shown in grey (inaccessible). The Ewald sphere is shown as a circle with $\mathbf{K_0}$ radius, cutting the $(0\,0\,0\,4)$ reciprocal lattice point. From [37]

2θ angles. A computer control system directs the movement of such goniometers in order to easily perform the exploration of the reciprocal space, as explained in the previous section.

The detector is a Xe proportional counter mounted after a Ge $(2\,2\,0)$ three-bounces analyzer, with an angular acceptance of $0.0034°$. The analyzer strongly reduces the intensity of the signal, as it has a very narrow angular acceptance. It is also possible set an *open* detector configuration without any analyzer to aid in the sample alignment phase, before the actual measurement.

The high degree of precision we manage to reach with the HR-XRD technique comes at the price of a strong reduction of the intensity of the incident beam. For this reason long acquisition times are needed to obtain significant statistic on the data we collect.

4.1.3 *Data analysis*

The average crystal lattice of our films may differ from the one of pure bulk lithium niobate either for compositional reasons or due to the elastic interactions between the GaN substrate upon which our film is grown.

The difference between our film and the reference lithium niobate lattice can be expressed with the aid of the mismatch tensor ξ_{ij}

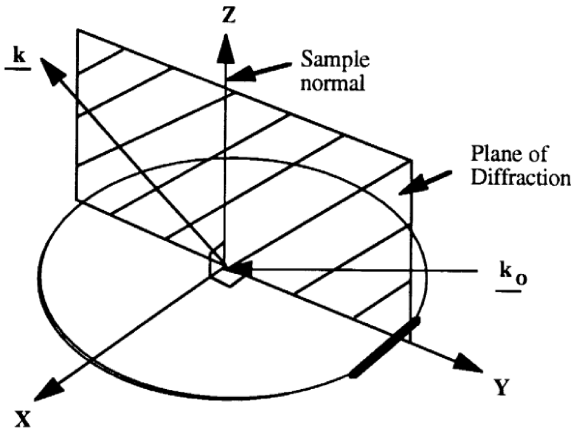

Figure 4.3: Schematic of an XRD measurement, highlighting the incident ($\mathbf{k_0}$) and outgoing ($\mathbf{k}$) x-ray wavevectors and the plane of diffraction. From [39]

Its general definition comes from the theory of elasticity and is the following:

$$\xi_{ij} = \frac{\partial u_i}{\partial x_j} \tag{4.5}$$

where u_i is a component of the deformation vector $\mathbf{u}$ which expresses the displacement of the layer's atom from their hypothetical positions matching the one of the reference lattice. The diagonal components can be written as:

$$\xi_{ii} = \frac{a_{L,i} - a_{S,i}}{a_{S,i}} \tag{4.6}$$

where $a_{L,i}$ is the i-th lattice parameter of the film, while $a_{S,i}$ is the corresponding parameter for the reference undistorted lattice.

It can be shown that the measured substrate-thin film mismatch ξ_{ij} can be expressed as the sum of the relaxed (free standing) substrate-thin film mismatch m_{ij} and of a strain tensor e_{ij}. The latter can be divided in the symmetric strain tensor ε_{ij} and the anti-symmetric rotation tensor ω_{ij}. [40]

$$\xi_{ij} = m_{ij} + e_{ij} = \tag{4.7}$$

$$= m_{ij} + \varepsilon_{ij} + \omega_{ij} \tag{4.8}$$

The ε_{ij} symmetric and ω_{ij} anti-symmetric tensors are defined as:

$$\varepsilon_{ij} = \frac{e_{ij} + e_{ji}}{2} \tag{4.9}$$

$$\omega_{ij} = \frac{e_{ij} - e_{ji}}{2} \tag{4.10}$$

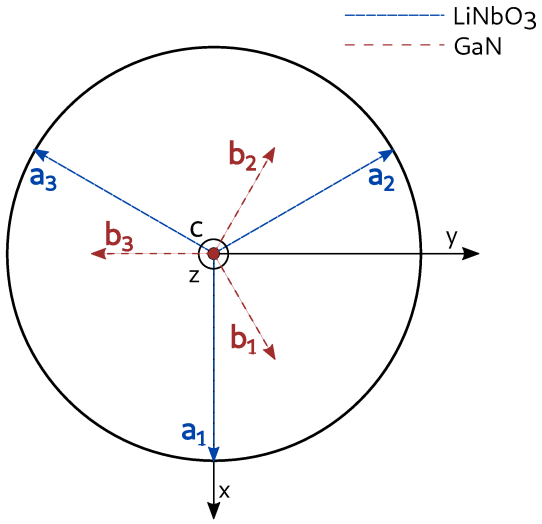

Figure 4.4: Diagram showing the relative orientation of the hexagonal lattice basis vectors for GaN and $LiNbO_3$ in a heterostructure obtained by epitaxial growth of $LiNbO_3$ on a GaN substrate.

The first step in our analysis is to obtain the measured mismatch tensor ξ_{ij}, to express the differences between the lithium niobate thin film and the bulk lithium niobate crystal.

In order to do so, we need to compute the $\Delta\mathbf{H}$ vectors first, which express the difference between the thin film and bulk lithium niobate reciprocal lattice vectors associated to a specific reflection.

As it is customary in RSM, the substrate reflections can be taken as an internal reference from which the lattice positions can be obtained with high precision. In this way, any unknown offset due to the actual sample mounting is removed. However, in our heterostructures, the substrate is constituted by GaN, so that our $\mathbf{\Delta H}$ vectors would be referred to some specific reciprocal lattice points (RLPs) of the GaN reciprocal lattice. Thus, in order to obtain the $\mathbf{\Delta H}$ with respect to the reference lithium niobate lattice, we can write:

$$\Delta\mathbf{H} = (\mathbf{H}_{LN}^{meas} - \mathbf{H}_{GaN}^{meas}) - (\mathbf{H}_{LN}^{ref} - \mathbf{H}_{GaN}^{ref}) \tag{4.11}$$

Once the $\Delta\mathbf{H}$ distances between RLPs are computed, one can proceed with the analysis.

We can rewrite the difference in the positions of the RLPs related to a specific reflection, for the thin film and the bulk crystal, as:

$$\mathbf{\Delta H} = -\boldsymbol{\nabla}(\mathbf{H}\cdot\mathbf{u}) = -\boldsymbol{\nabla}(H_{\parallel}u_{\parallel} + H_{\perp}u_{\perp}) \tag{4.12}$$

where, in the second equation, we have decomposed the vector along two directions, parallel and perpendicular to the interface plane. Using

the definition of the measured mismatch tensor ξ_{ij}, Equation 4.5, we obtain the two equations:

$$\begin{cases} \Delta H_{\parallel} = & -\xi_{\perp,\parallel} H_{\perp} - \xi_{\parallel,\parallel} H_{\parallel} \\ \Delta H_{\perp} = & -\xi_{\perp,\perp} H_{\perp} - \xi_{\parallel,\perp} H_{\parallel} \end{cases} \tag{4.13}$$

Those two equations give us an easy way to measure the mismatch tensor. Selecting a sufficient number of independent reflections, each lying in some plane along the Cartesian axes x, y, z, we can isolate the various components of the tensor.

We chose three reflections. A first one LN $(0\,0\,6)$ placed along the surface normal, $(0\,3\,\bar{1}\,2)$ lithium niobate lying in the yz plane and the third one $(2\,\bar{1}\,\bar{1}\,2)$ lithium niobate in the xz plane, as can be seen in the stereographic projection in Figure 4.5.

The first measurement is the lithium niobate $(0\,0\,6)$ reflection, with the scattering plane (i. e. the plane defined by the $\mathbf{K_0}$ and $\mathbf{K_h}$ vectors) parallel to the y and z directions. The measurement of the position of the $\mathbf{H}^{(006)}$ vector, decomposed along the z and y axes gives us information about the zz, yy, zy and yz components of the ξ tensor:

$$\begin{cases} \Delta H_y^{(006)} = & -\xi_{z,y} H_z^{(006)} - \xi_{y,y} H_y^{(006)} = -\xi_{z,y} H_z^{(006)} \\ \Delta H_z^{(006)} = & -\xi_{z,z} H_z^{(006)} - \xi_{y,z} H_y^{(006)} = -\xi_{z,z} H_z^{(006)} \end{cases} \tag{4.14}$$

However, due to the $\mathbf{H}$ having null y component, we don't obtain information on the yy and yz components of the tensor from this reflection.

In a similar way, we can set two equations for each of the other reflections and obtain the following system:

$$\begin{cases} \Delta H_y^{(006)} &= -\xi_{z,y} H_z^{(006)} \\ \Delta H_z^{(006)} &= -\xi_{z,z} H_z^{(006)} \\ \Delta H_y^{(0\bar{3}12)} &= -\xi_{z,y} H_z^{(0\bar{3}12)} - \xi_{y,y} H_y^{(0\bar{3}12)} \\ \Delta H_z^{(0\bar{3}12)} &= -\xi_{z,z} H_z^{(0\bar{3}12)} - \xi_{y,z} H_y^{(0\bar{3}12)} \\ \Delta H_x^{(2\bar{1}\bar{1}2)} &= -\xi_{z,x} H_z^{(2\bar{1}\bar{1}2)} - \xi_{x,x} H_x^{(2\bar{1}\bar{1}2)} \\ \Delta H_z^{(2\bar{1}\bar{1}2)} &= -\xi_{z,z} H_z^{(2\bar{1}\bar{1}2)} - \xi_{x,z} H_x^{(2\bar{1}\bar{1}2)} \\ \Delta H_x^{(006)} &= -\xi_{z,x} H_z^{(006)} - \xi_{x,x} H_x^{(006)} \\ \Delta H_z^{(006)} &= -\xi_{z,z} H_z^{(006)} - \xi_{x,z} H_x^{(006)} \end{cases} \tag{4.15}$$

We can write such system (Equation 4.15) using matricial notation, as:

$$\Delta \vec{H} = H \vec{\xi} \tag{4.16}$$

where $\Delta \vec{H}$ is a vector containing the various components for the reflections differences, along the various directions, while H is a

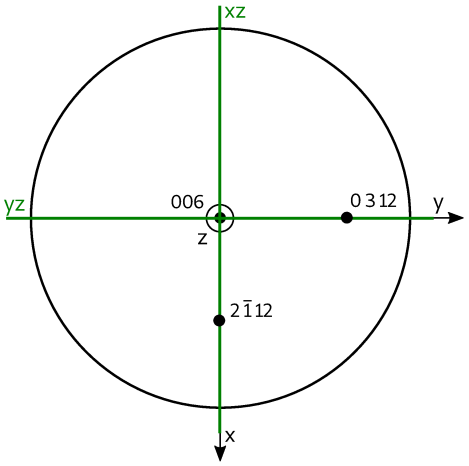

Figure 4.5: Stereographic projection of a sphere in real space, showing the intersections with the vectors associated to the $(0\,0\,6)$, $(0\,3\,12)$ and $(2\,\bar{1}\,12)$ planes as points. The reciprocal space vectors related to these reflections are shown respectively in Figure 4.6a, Figure 4.6b and Figure 4.6c. The diffraction planes in which the measurements are performed are the xz and yz planes, highlighted in green.

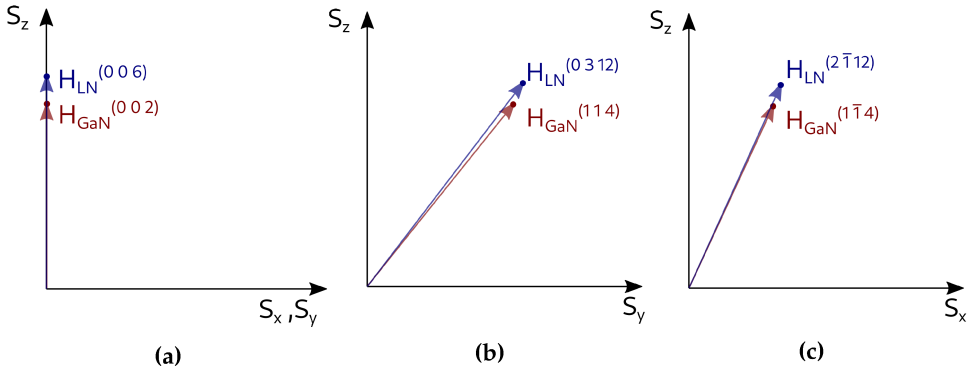

Figure 4.6: Position of reciprocal lattice points for $LiNbO_3$ and GaN reflections of interest in our study.

matrix containing the various coordinates for the reflections, along the various directions and $\vec{\xi}$ is a vector with the components of the ξ_{ij} tensor. Multiplying for the inverse of such matrix, we can obtain the vector with the components of the mismatch tensor as:

$$\vec{\xi} = H^{-1}\Delta\vec{H} \tag{4.17}$$

This way, we were able to reconstruct 7 out of the 9 components of the mismatch tensor ξ, with the exclusion of the xy and yx components, which we were not able to measure in our experiment.

Table 4.1: Fe:$LiNbO_3$ thin-film/bulk $LiNbO_3$ mismatch tensor components for various samples analyzed in this thesis.

ξ_{ij}	P_1	P_2	P_3	N_1	N_2	N_3
xx	$-0.089(5)$	$-0.081(5)$	$-0.083(5)$	$-0.081(5)$	$-0.081(5)$	$-0.082(5)$
yy	$-0.078(3)$	$-0.082(3)$	$-0.084(3)$	$-0.082(3)$	$-0.082(3)$	$-0.082(3)$
zz	$-0.0726(5)$	$-0.0677(3)$	$-0.0678(9)$	$-0.0677(8)$	$-0.0677(8)$	$-0.067(2)$
xz	$0.008(3)$	$-0.003(2)$	$-0.002(3)$	$-0.003(3)$	$-0.003(3)$	$-0.003(4)$
zx	$0.006(2)$	$0.002(2)$	$0.001(2)$	$0.003(2)$	$0.002(2)$	$0.003(2)$
yz	$0.004(2)$	$-0.002(2)$	$-0.001(2)$	$-0.002(2)$	$-0.002(2)$	$-0.003(2)$
zy	$-0.001(2)$	$0.0004(20)$	$0.001(2)$	$0.002(2)$	$0.001(2)$	$0.002(2)$

4.1.4 *Results*

The mismatch tensor was obtained for all the Fe:$LiNbO_3$ samples synthesized and showed no significant differences between the various samples. In Table 4.1 the components of the mismatch tensor are reported for all the samples. Uncertainties on these data were computed by propagating the uncertainties on the position of goniometers on the setup, needed to measure a certain reflection. Such uncertainties are the combination of a statistical uncertainty on the determination of the centroid of the specific reflection peaks and an uncertainty due to the accuracy of goniometer positioning system.

This data shows a -7% deformation along the z crystal direction, with basically no shear components (xz, zx, yz, zy components are basically zero, within the uncertainties). As for the components in the xy plane, a deformation of -8% is generally found.

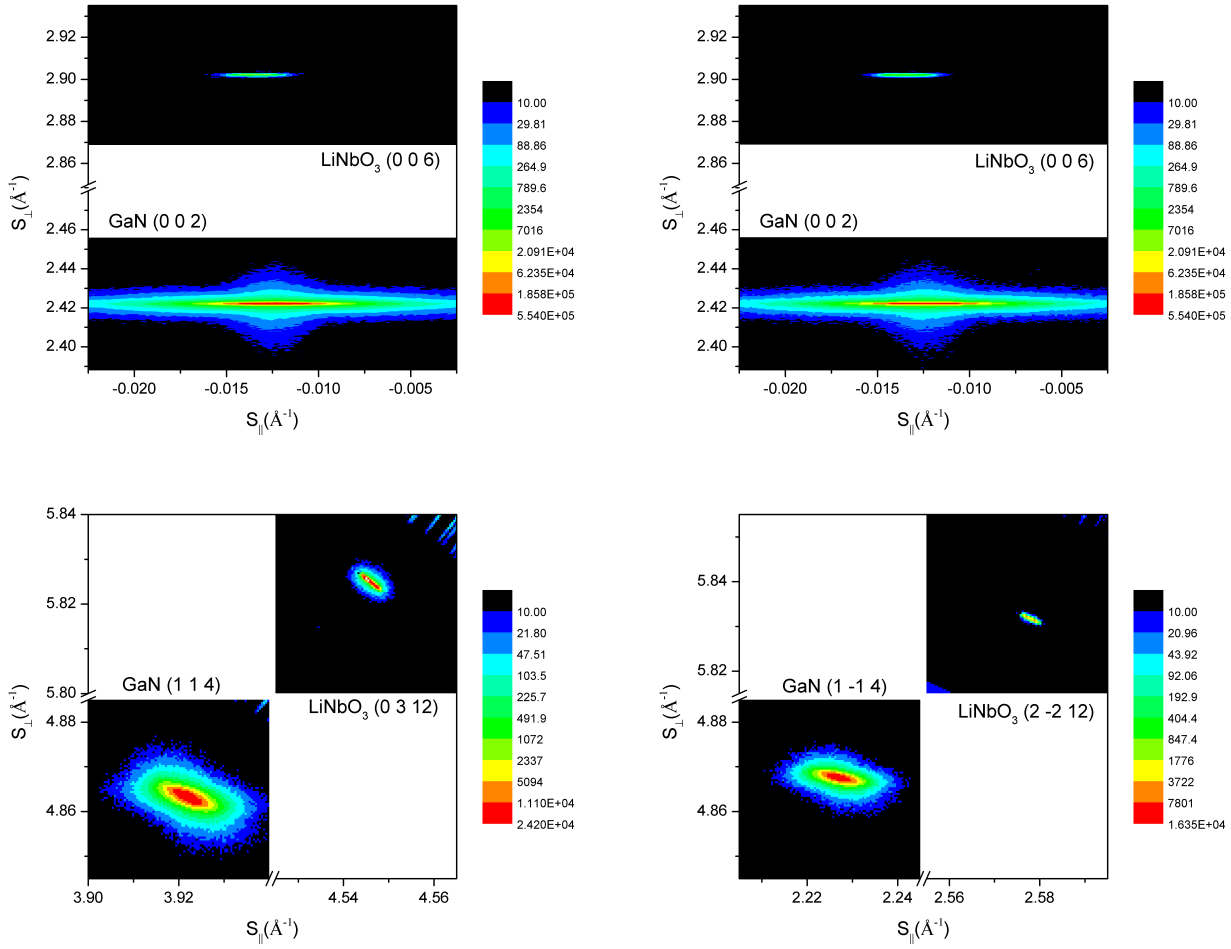

Figure 4.7: Measured reciprocal space maps of $LiNbO_3$ and GaN reflections of interest, for sample N1.

4.2 COMPOSITIONAL ANALYSIS

In order to test the results of the deposition technique, compositional analysis was performed on each of the synthesized samples using ion beam characterization methods. The techniques used were *Rutherford Backscattering Spectrometry* (RBS) for the niobium concentration and *Nuclear Reaction Analysis* (NRA) for the lithium concentration.

Ion beam analysis comprehends a wide range of surface characterization techniques, which probe the material properties by measuring its response to an incoming beam of energetic ions.

In the case of RBS, the measured signal comes from the detection of backscattered ions from elastic collisions with the atomic nuclei of the target material. In the NRA case, energetic ions induce specific nuclear reactions in the material and the reaction products, either nuclei or emitted radiation are measured to infer the presence of the target element.

RBS and NRA measurements were performed by Davide De Salvador and Francesco Sgarbossa at the LNL AN2000 and CN accelerator facilities at INFN Legnaro National Laboratory (INFN-LNL).

4.2.1 *Rutherford Backscattering Spectrometry*

INTRODUCTION This quantitative analysis technique probes the sample's structure and composition by sending an accelerated ion beam to impinge on its surface. The measurement of the energy and number of the backscattered ions provides quantitative information about the sample's composition and density, with penetration depth up to several hundreds of nm in the material. It is a non-destructive technique which requires minimal calibration and for these reasons it is widely adopted in semiconductor research.

The measured signal is the backscattered ion *yield* Y, which can be modeled as:

$$Y = Q_D = Q N_s \, \sigma(\theta) \, \Omega \tag{4.18}$$

where Q and Q_D are respectively the number of incoming and detected ions (assuming 100% detection efficiency), N_s is the sample's atomic density, Ω is the detector's solid angle and $\sigma(\theta)$ is the scattering cross section at θ angle with respect to the incoming beam direction, integrated over the detector solid angle. The N_s density is an *areal* density, which can be computed from the atomic *volume* density and thickness as $N_s = N\, t$ if the sample is homogeneous.

For the typical energy range used in RBS experiments (2 MeV $^4He^+$ ion beams) the collision is an elastic process, in which the total kinetic energy is conserved, resulting from Coulomb interaction between

the incoming ions (Q) and the atomic nuclei of the sample (N_s). In this case, the differential cross section can be computed by imposing momentum and energy conservation and results in the well known Rutherford cross section:

$$\sigma(\theta) = \left(\frac{Z_1 Z_2 e^2}{4E}\right)^2 \frac{1}{\sin^4(\theta/2)} \tag{4.19}$$

where Z_1, Z_2 are the ion and target nuclei atomic numbers, E is the incoming ion energy and e is the electron charge. [41]

This kind of elastic interaction happens for incoming ions with kinetic energy in the MeV range, as ions at lower energies or interacting with heavy nuclei cannot fully penetrate the electron cloud and therefore do not experience the full Coulomb potential of the nucleus but a partially screened one, due to the inner-electrons' charge screening.

At certain energies and ion-target pairs the scattering process is not elastic as the ion and the target nuclei take part in nuclear reactions, especially for energetic beams of several MeV. This is used in Nuclear Reaction Analysis (subsection 4.2.2), a set of techniques which can be useful to obtain sensitivity to certain elements, especially lighter elements to which RBS has limited sensitivity.

In the collision energy and momentum are exchanged between the moving ion to the stationary target. Since the energy and momentum of the probe ion beam are known, by measuring the same quantities for the backscattered ions it is possible to obtain information on the collision, and in particular on the masses of the target atoms.

Under the elastic interaction assumption, both momentum and kinetic energy are conserved in the system composed of the incoming ion and of the atomic target. This way the out-coming ion energy E_1 can be easily related to the incoming beam energy E by the *kinematic factor* K, defined as their ratio, which can be expressed as:

$$K = \frac{E_1}{E} = \left[\frac{(M_2^2 - M_1^2 \sin^2\theta)^{1/2} + M_1 \cos\theta}{M_2 + M_1}\right]^2 \tag{4.20}$$

This expression is valid for projectiles lighter than the target atoms $M_1 < M_2$. This expression shows that the ratio only depends on the projectile (M_1) and target atom (M_2) masses and on the scattering angle θ.

When scattering happens on the material's surface, E is equal to the incident beam energy E_0. However, the ion beam can penetrate the material and lose some of its energy before a scattering event, emerging with an energy lower than ions backscattered at the surface of the material. Therefore, in order to model and understand properly

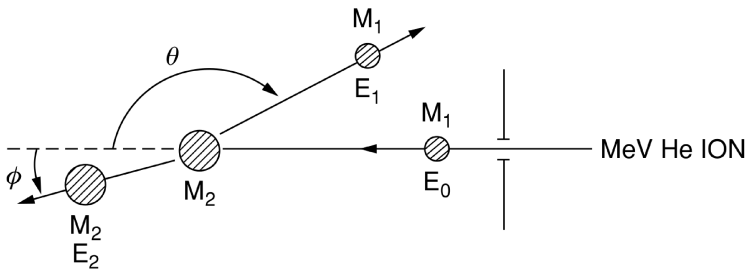

Figure 4.8: Schematic of the ion-target collision in an RBS experiment. From [41]

the signal in an RBS experiment, models of ion's energy loss in the material must be developed.

For light ions such as H^+ or $^4He^+$ at the MeV energy, energy loss in the material is mostly due to excitation and ionization of atomic electrons in inelastic collisions with them (*electronic energy loss*).[2] We can develop a *stopping power* coefficient $\frac{dE}{dx}$ to macroscopically describe this continue energy loss of energetic ions moving in a material. The value of such coefficient depends on the ion energy, the ion and target atomic numbers and are reported in large empirically-derived databases [42].

The energy before the scattering event can be expressed as the initial beam energy minus the energy loss experienced by the ion from the surface up to the depth t at which the scattering event happens:

$$E(t) = E_0 - \Delta E_{in} = E_0 - \int_0^t \frac{dE}{dx}\, dx \tag{4.21}$$

After the elastic scattering event at t depth, the energy of the out-going particle can be expressed as:

$$E_1(t) = KE(t) - \Delta E_{out} = KE(t) - \int_0^{\frac{t}{\cos\theta}} \frac{dE}{dx}\, dx \tag{4.22}$$

This is the energy measured by an energy-resolved detector in an RBS experiment and used to build energy-yield plots, such as Figure 4.9.

The types of information that can be extracted from such measurements are:

- Atomic mass of the target atoms: backscattered ion energy provides this information about the elements composing the sample.
- Total amount of an atomic specie in the material (*dose*): integration of the yield signal over all the energies related to specific

2 At lower energies, interaction with the atomic nuclei results in *nuclear energy loss* being the main energy loss mechanism.

element peak in the energy-yield plot provides information over the scatterers density N_s in that layer. For an indefinitely thin layer Equation 4.18 is valid, while for thicker layers, a simulation of the spectrum is required.

- Thickness of the layers in the material: once an atomic volume density of the layer's material is assumed, thickness of the material can be obtained. Simulation is commonly used to take into account the effect of the change in stopping power due to the energy loss in the material.

- Crystalline quality of the material: in the case of a high-quality single-crystal target, by aligning the ion beam direction with a sample's crystalline direction, it is possible to observe a reduction in the back-scattering yield, due to an effect known as *channeling*. This effect is due to a *steering* action of the atomic nuclei rows along a crystal axis, which confines the incoming ions trajectory in a channel, limiting their chances to interact and backscatter with the atomic nuclei in the material. Such phenomenon strictly depends on the sample's crystalline quality. [41]

EXPERIMENTAL DETAILS Measurements were performed on several samples:

- Run 1 Fe:$LiNbO_3$ on p-GaN samples (P1, P2, P3)

- Commercial Smart Cut Fe:$LiNbO_3$ samples (Fe:$LiNbO_3$ SC)

- Commercial Smart Cut congruent $LiNbO_3$ samples (cLN SC)

Measurements on the last two types of samples were performed in order to have some reference results for comparison with the ones we synthesized.

Commercial Fe:$LiNbO_3$ samples were produced by NanoLN company[3] as mono-crystalline thin films, using the *Smart Cut* technique. This technique is used to produce thin films by performing ion implantation at a certain depth in a bulk crystal, which results in the formation of an amorphous layer in the material at a desired and reproducible depth. The implanted wafer is then flipped on the top of the desired substrate and a thermal treatment is performed. The amorphous layer therefore separates from the sacrificial wafer leaving on the top of the final substrate a peeled crystalline film of controlled thickness. The advantage of this technique is that it allows the deposition of high quality crystal layers on heterogeneous substrates, which would be impossible using bottom - up approaches such as epitaxial growth. [43]

3 https://www.nanoln.com/

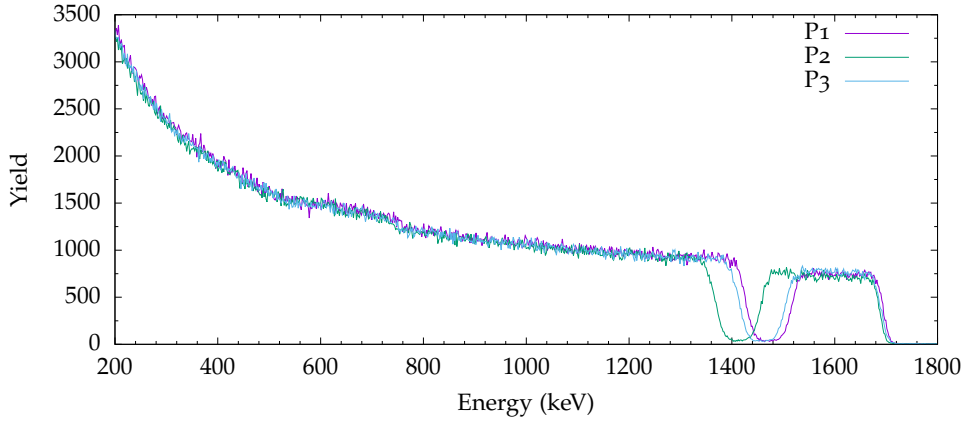

Figure 4.9: 2 MeV $^4He^+$ RBS spectrum showing yield as a function of backscattered ion energy, for Fe:$LiNbO_3$ samples grown on p-GaN.

These Fe:$LiNbO_3$ Smart Cut samples are a multilayer structure of 300 nm Fe:$LiNbO_3$ (0.2 % mol Fe), 30 nm Cr, 100 nm Pt, 10 nm Cr on a SiO_2 on bulk LN substrate. They are oriented with the $(0\,0\,L)$ direction perpendicular to the major surface.

For the measurements a $^4He^+$ beam was used, accelerated at beam energies of 2 and 4.2 MeV, using the AN2000 and CN accelerators. Si detectors with resolution of 20 and 18 keV were placed at $\theta = 160°$ respectively in the AN2000 and CN accelerator configurations.

The RBS spectra were calibrated in energy by measuring the channels number associated to the surface backscattering peaks for several samples of known composition, used as standards. Once a correspondence between such channels and the surface backscattering energies KE_0 was set, the spectra were energy calibrated by performing a linear fit interpolation. The samples used were AuSi, SiO_2 and C, chosen in order to cover a wide range of atomic masses and therefore a wide range of backscattering energies in the spectra.

The spectra were also calibrated with respect to the detector solid angle, which affects the measurement of the backscattering yield (Equation 4.18), by using another standard sample of known dose, composed of TaSi.

DATA ANALYSIS The RBS spectrum of one of our expitaxially grown Fe:$LiNbO_3$ thin films is shown in Figure 4.9. We can see the Nb signal due to the Fe:$LiNbO_3$ thin film (1700 keV), the Ga signal from the GaN substrate (1400 keV) and on top of it the O signal from Fe:$LiNbO_3$ (730 keV). Due to the low concentration, the Fe impurity in Fe:$LiNbO_3$ cannot be detected by RBS measurements. Due to its light mass, lithium produces an RBS signal at very low energy, which cannot be

Table 4.2: Nb dose measurements and density calculation for various samples analyzed in this thesis.

Sample	$dose_{Nb}$ [$\times 10^{15}$at/cm^2]	n_{Nb} [$\times 10^{22}$at/cm^3]	$n_{Nb}/n_{Nb}^{ref.}$ %
P1	443(20)	2.2(3)	119(13)
P2	558(20)	1.9(1)	100(6)
P3	459(20)	2.2(2)	107(10)
Fe:$LiNbO_3$ SC	587(30)	1.9(1)	107(5)
Fe:$LiNbO_3$ SC	597(30)	2.0(1)	109(5)
cLN SC	1340(70)	1.87(9)	100(5)
cLN ref.	/	1.862	100

detected in our RBS setup and would sit on top of the large tail of the Ga signal.

Information about the Nb concentration in the sample was obtained starting from dose measurements. Using film thickness values measured with other techniques (section 3.6) we can obtain an estimate of the atomic volume density of the material by dividing the dose N_s by the film thickness. We can compare this data with the reference atomic volume density for Nb in cLN, obtained from the material's mass density. Such data is reported in Table 4.2. In this table dose measurements are reported for 3 Run 1 samples (P1, P2, P3) deposited with different deposition conditions on a p-GaN substrate. Additionally, three reference samples were also measured: two Fe:$LiNbO_3$ Smart Cut samples sourced from different areas of the same wafer and a cLN Smart Cut one.

Uncertainty for dose measurements can be attributed to two factors: statistical uncertainty in the counting of backscattered ions and uncertainty in the measurement of the detector's solid angle. With these two sources of error taken into account, the dose measurements carry a 5% uncertainty.

The atomic density estimates strongly depends on the assumed thickness value for the thin film, whose uncertainty must be combined with the dose measurements uncertainty. This results in density estimation uncertainties around 10% for Fe:$LiNbO_3$ samples on p-GaN, due to the 10% uncertainty in profilometry thickness measurements. For Fe:$LiNbO_3$ and cLN SC samples uncertainty amounts to 5%, in line with the dose measurements uncertainty, owing to the manufacturer's thickness measurements having small uncertainty (<1%).

For certain samples, RBS measurements were performed in different zones of the sample. When possible a weighted average of those results was computed and this reduced the uncertainty in the final estimates.

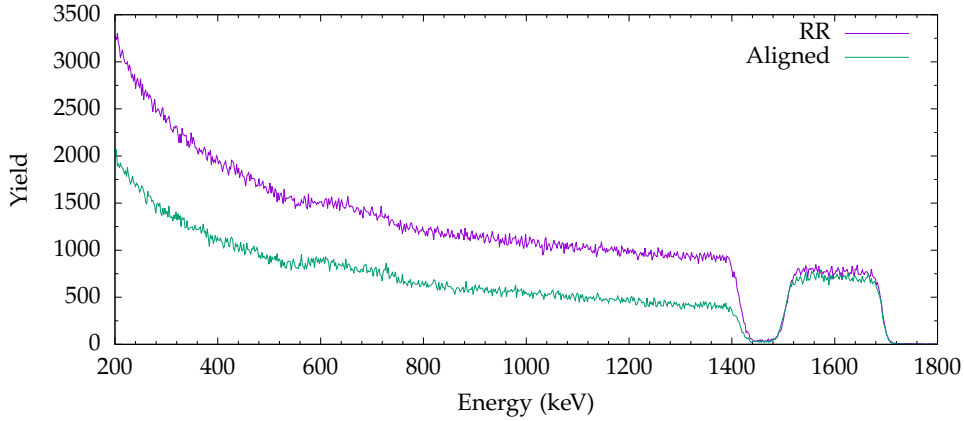

Figure 4.10: 2 MeV $^4He^+$ RBS spectra of P3 sample in *Random Rotating* configuration (RR) and aligned with the GaN substrate $(0\,0\,1)$ axis, showing a yield reduction of the Ga signal due to channeling effects.

RESULTS From the atomic density data we can notice that most of the samples have a Nb density compatible with the congruent LN value within experimental uncertainty. The only noticeable exception being the Fe:$LiNbO_3$ P1 sample which shows an excess in Nb compared with cLN value, well over the uncertainty range.

Additionally, RBS channeling measurements were performed, by aligning the beam direction with the GaN substrate $(0\,0\,1)$ direction. We can notice a significant reduction in yield for Ga signal but only a limited reduction for Fe:$LiNbO_3$'s Nb signal as shown in Figure 4.10.

This hints to the presence of a significant amount of structural defects in the Fe:$LiNbO_3$ film. Since from HR X-ray diffraction data we have evidence of a highly oriented lattice with narrow diffraction peaks, a possible explanation for this observation is that our film is characterized by a high density of threading dislocations favoring the beam dechanneling in the LN film.

4.2.2 *Nuclear Reaction Analysis*

Due to the inability to measure the lithium dose in our samples with RBS, another ion beam technique was used to measure the concentration of this light element.

INTRODUCTION Nuclear Reaction Analysis is an ion beam technique similar to RBS. An accelerated ion beam is directed towards the surface of the sample. The ion type and energy are selected in order to induce specific nuclear reactions with the target nuclei. The reaction products, either ejected product nuclei or high-energy radiation are measured with energy resolved detectors. This signal is used to infer the presence and concentration of specific elements in the material.

The measured signal can be related to the number of target atoms in the material by Equation 4.18, with Q_D being in this case the number of reaction products and not the backscattered ions. The reaction cross section for NRA depends on the specific nuclear reaction involved and are reported in databases such as IBANDL. [44]

Depending on the nuclear reaction cross section's variation with energy and on the material's stopping power for the incoming and emitted nuclei, the NRA spectrum can be used to perform depth profiling of the target element in a sample. As an example, if the reaction has a cross section resonance at a specific energy, the beam energy can be increased from that value to probe concentration of the target nuclei at increasing depth.

EXPERIMENTAL DETAILS Our NRA measurements employed the ^{7}Li(p,α)^{4}He nuclear reaction, with a Q value of $Q = 17.34\,\text{MeV}$, whose main products are two ^{4}He nuclei of 7.7 MeV energy. [41, 45]

A 1.6 MeV proton (p) beam was directed at the sample and a Si detector was placed at an θ =150° with respect to the incident beam direction and measured the $^{4}He^{2+}$ ions produced in the nuclear reaction. The detector was covered with a mylar film, in order to prevent the low-energy backscattered protons to reach the Si detector.

As for depth profiling with NRA measurements, in our case the reaction cross section does not significantly vary with energy at the chosen p energy (no resonance). [46] As the proton energy loss in the material not high it is not simple to extract depth information from this kind of experiment. For these reasons we decided to measure the $^{4}He^{2+}$ production at constant beam energy. The NRA signal in our experiment does not carry significant depth profiling information and instead provides information about the total target element concentration in the thin film.

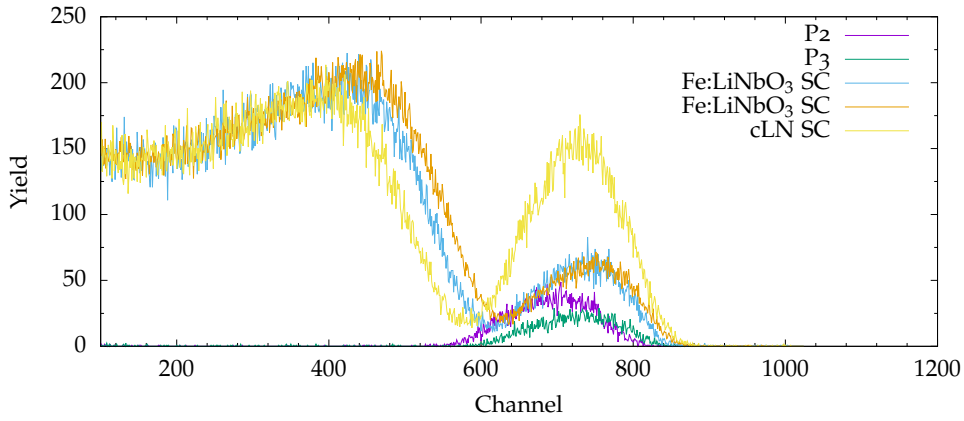

Figure 4.11: NRA spectrum showing $^4He^{2+}$ product nuclei yield as a function of their energy, for Fe:$LiNbO_3$ samples grown on p-GaN, Fe:$LiNbO_3$ and cLN Smart Cut samples. Channel number is directly proportional to energy.

DATA ANALYSIS A plot of the NRA spectra for Fe:$LiNbO_3$ samples on p-GaN is reported in Figure 4.11, along with spectra relative to Fe:$LiNbO_3$ and cLN Smart Cut samples.

In all these NRA spectra we can see a peak corresponding to the lithium in the lithium niobate thin films, between detector channel 600 and 800. We can see that the NRA signal for Smart Cut samples shows this first sharp peak followed by a second, wider peak, at lower energies. This is representative of the fact that the impinging protons activate the reaction both in the superficial LN thin film and in the bulk LN substrate in these samples. The separation between the peaks is due to the presence of Cr/Pt/Cr layers in between them, which have the effect of reducing the outgoing ^4He ions energy.

The lithium dose in the various samples is proportional to the integral of the thin film peak of the $^4He^{2+}$ signal, as this is a product nucleus of the reaction, having a well defined energy around 7.7 MeV.

The uncertainty of the integral value is only of statistical nature and reflects the counting error on the measured product nuclei number. This uncertainty is around 1% in our measurements.

The lithium atomic density in the various samples was estimated by comparing the integral of the peak, normalized by the film thickness, to the one of a reference undoped thin film sample which we assume to have a Li atomic density of 1.862×10^{22} at/cm^3, corresponding to congruent LN stoichiometry. As the experimental setup was the same, the detector's solid angle and the scattering cross section did not influence the ratio of such integrals.

To estimate lithium atomic density, we made the assumption that the integral of the cLN thin film signal, normalized by film thickness, was

Table 4.3: Li concentration and density estimates for various samples analyzed in this thesis.

Sample	Int_{Li} [10^3 #/charge]	n_{Li} [$\times 10^{22}$at/cm^3]	$n_{Li}/n_{Li}^{ref.}$ %
P1	3.77(6)	1.06(3)	57(15)
P2	5.17(6)	0.96(9)	52(5)
P3	3.27(5)	0.85(2)	46(10)
Fe:$LiNbO_3$ SC	9.09(9)	1.72(2)	93(1)
Fe:$LiNbO_3$ SC	9.32(6)	1.76(2)	95(1)
cLN SC	23.9(2)	1.86(1)	100(1)
cLN ref.	/	1.862	100

related to the reference value of lithium's atomic density in $LiNbO_3$. Li atomic density for the other thin film Fe:$LiNbO_3$ samples was then estimated using the ratios between the normalized integrals.

As in the RBS analysis, this estimation of atomic density is affected by the thickness value used for the normalization and this factor carries significant uncertainty. Propagating such uncertainties results in uncertainties around 10% for the Fe:$LiNbO_3$ on p-GaN samples, while for Smart Cut samples uncertainties were close to 1%, due to the reduced uncertainty in the manufacturer's thickness values.

As in RBS, NRA measurements were performed in different zones of the sample in many cases. Whenever possible a weighted average of those results was evaluated and this lowered the uncertainty in the final measurements.

RESULTS Our data indicate that the samples produced by RF magnetron sputtering are strongly sub-stoichiometric, which is in agreement with previous reports. [27] In particular the Li content is about 50% of the cLN value. A role can also be ascribed by the strong Fe doping of our samples, which needs to be better investigated. Additionally also the Fe:$LiNbO_3$ Smart Cut samples have a slight lithium deficiency, which could be partly attributed to the Fe doping.

4.2.3 *Lithium-niobium ratio*

The atomic density computations in the previous two sections provide a way to estimate Li and Nb concentration in the samples, but are strongly affected by film thickness measurements. It is possible to avoid such dependence by computing the [Li]/([Li]+[Nb]) dose ratio as this value does not depend on the sample's thickness. Values of this parameter are reported in Table 4.4.

As in NRA measurements the Li signal integrals were obtained and the relative dose was not estimated by simulation, we proceeded to

Table 4.4: [Li]/([Li]+[Nb]) ratio for various samples analyzed in this thesis.

Sample	[Li]/([Li]+[Nb]) %
P1	30.9(1)
P2	32.8(1)
P3	27.3(1)
Fe:$LiNbO_3$ SC	44.9(1)
Fe:$LiNbO_3$ SC	44.5(1)
cLN SC	48.5(1)
cLN ref.	48.5

estimate it in the following way. Given the measured Nb dose of the cLN SC sample, we computed the corresponding Li dose, assuming the Li was present in the cLN ratio (48.5% [Li]/([Li]+[Nb])).

Once this reference value was obtained for Li, we proceeded to convert the Li signals integrals for the other samples to dose values, by rescaling the cLN reference dose value by the ratio between the corresponding integrals of the selected samples and the cLN SC sample.

As the Li atomic density estimation suggested, the Fe:$LiNbO_3$ on p-GaN thin film appears to be greatly below the congruent [Li]/([Li]+[Nb]) ratio, which, as the Nb density measurement testify, is to be connected to an higher Nb density only for the P.3 sample. Therefore the low [Li]/([Li]+[Nb]) ratio is mostly due to a significantly lower Li density.

Compositional analysis is crucial for studies on $LiNbO_3$'s properties as Li, Nb and defect densities have a significant impact on them, as explained in subsection 2.1.4.

4.3 UV-VIS ABSORPTION SPECTROSCOPY

In order to obtain information on film thickness and on the optical properties of the deposited films, UV-Vis-NIR absorption spectroscopy was performed on the samples. [21]

Optical absorption measurements were performed as transmission measurements, in which the sample was illuminated by a monochromatic light source and the transmitted light intensity was collected. By normalizing such spectra with a *baseline* spectrum recorded without the sample, we were able to measure the absolute transmission coefficient at that wavelength. We performed such measurements in a wide range of wavelengths, from UV to NIR.

A detailed analysis of such spectra can explain its features at different wavelengths and yield insight on the sample's composition, as in transparent materials absorption is often related to impurities and defects. In particular, Fe^{2+}impurities in lithium niobate give rise to a broad absorption band peaked around 532 nm which can be used to obtain information on the Fe concentration and on its reduction degree. [21] Additionally, thin film transmission spectra often shows characteristic interference patterns which can be analyzed to provide thin film thickness estimations.

4.3.1 *Experimental details*

The measurements were performed using a JASCO V670 UV-Vis spectrophotometer, in the 350-2500 nm wavelength range, at 1 nm steps. In order to resolve the fast oscillations in the UV region of our spectra, measurements were carried with spectrophotometer set to narrow spectral bandwidth 0.1 nm in the UV-Vis region.

In each measurement session, the detector's *dark* response was measured with the source covered and the sample missing. This was used for calibration of the detector, to avoid spurious detection in the samples' actual measurements.

A baseline spectrum was acquired by performing a measurement with the light source on but the sample missing, to characterize the light source or the spectral response of the detector to our light source. For each measurement this baseline was used to normalize the measured intensity and to obtain the absolute transmittance data.

Before the measurements, the samples were cleaned with the standard cleaning procedure, as explained in section 3.5.

As only the n-GaN on sapphire substrates were double polished, optical transmission measurements were only possible on such samples. As the samples were deposited on one p- and one n-GaN substrate in

the each sputtering run, we can assume that the results obtained from this analysis, such as the lithium niobate thin film thickness, will be valid for both samples.

4.3.2 *Data analysis*

In our experiment a monochromatic light source propagates in a multilayered medium, each layer being characterized by different refractive indices n_i and thicknesses d_i. At each interface between different mediums, the incident beam splits in a transmitted and a reflected component, according to Fresnel's laws. In a multilayered material, the waves can undergo multiple reflections and, if the wave's coherence length is longer than the layer thickness, different reflections of the wave can interfere as it happens in a Fabry-Perot interferometer.

This phenomenon makes computing the amplitude of the transmitted and reflected waves a non-trivial task, as soon as the system is composed of more than one layer. For this reason, a simple and easily scalable approach was devised, called the *Transfer Matrix Method* (TMM). [47] Details of such formalism are provided in Appendix A. A code was developed in the Python programming language to implement such method and it was used to simulate the experimental curves.

The core idea of the method is to define a 2D vector with the forward and backward propagating complex field amplitudes composing the light wave, where E_i^+ represents the forward propagating wave and E_i^- the backward propagating one. The effect of each interface between different media and layer medium on the light wave is encoded in a set of matrices, one for each interface or layer. Matrix multiplication of such matrices elegantly takes into account all of the possible combinations of reflection and transmission between the layers and results in a single transfer matrix T which models the whole multilayer's optical response, so that the light amplitude after the n-th layer $E_{N+1}^{\pm}$ can be related to the incoming light amplitude $E_0^{\pm}$ as:

$$\begin{pmatrix} E_0^+ \\ E_0^- \end{pmatrix} = T_{0/N+1} \begin{pmatrix} E_{N+1}^+ \\ E_{N+1}^- \end{pmatrix} \tag{4.23}$$

By tuning the thickness, absorption parameters of the layers and the roughness of the interfaces it is possible to develop accurate models which closely match the experimental transmission spectra. We decided to use the real part of the refractive indices n from the following literature data: [48] for sapphire and GaN, [49] for cLN. The complex part of the refractive index, k was computed from the absorption coefficient α as $k = \alpha \frac{\lambda}{4\pi}$.

The model of the Fe:$LiNbO_3$ on GaN samples is composed by three layers: a lithium niobate thin film grown on a GaN on sapphire substrate.

To decouple lithium niobate's absorption from the substrate, an analysis of the GaN on sapphire substrate was performed first. A model of the substrate was developed and its simulation was compared to the experimental data.

GAN ON SAPPHIRE SUBSTRATE In the experimental spectra (Figure 4.13a) we can notice that the substrate is transparent from NIR to the UV region, up to its absorption edge around 3.4 eV, which matches GaN's room temperature band gap. [48]

A striking feature of such spectra is a variable-period oscillation which modulates the transmission signal in the transparent region, resulting in a maximum oscillation between 70 and 80 T%. This oscillation was found to originate from thin-film interference in the GaN film and its period is closely linked to the thickness of the film.

The amplitude of these oscillations is almost constant in the NIR region and decreases in the UV region. This effect can be explained as due to the interface roughness, which increasingly affects light waves at smaller wavelengths, as the field oscillations happen on a length scale closer to the order of magnitude of the roughness of the film.

To be more precise, this effect can to be attributed to any random fluctuations of the optical path, affecting in a position-dependent manner the phase of the beam. Therefore this effect can be due either to the presence of roughness (intended as a position-dependent random variation of the layer thickness), either to a non homogeneous refractive index inside the film. As we cannot distinguish between those two situations, in the following we will refer to this effect as "roughness" for sake of simplicity.

In the NIR region, one can also notice high-frequency oscillations modulating the transmission signal. Such oscillations, which our apparatus can resolve only in the NIR region, as their period is larger in that region, are interference fringes due to the sapphire substrate.

The absorption edge is characterized by an exponential increase in absorption, which quickly reduces transmission to zero. This region can be modeled using an energy dependent absorption function. We chose to use an exponential model, called *Urbach model*. In this model, the spectral dependence of the absorption coefficient, in the edge region is:

$$\alpha(E,T) = \alpha_0 \exp\left(\frac{E - E_0}{E_U(T)}\right) \tag{4.24}$$

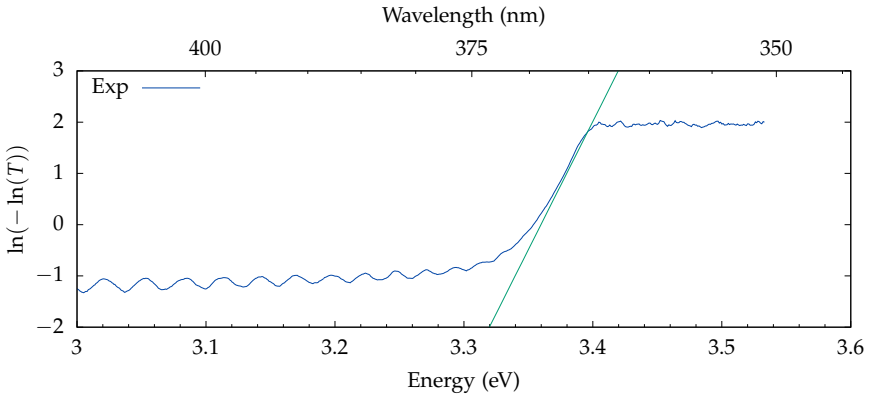

Figure 4.12: $\ln(-ln(T))(E)$ plot of n-GaN on sapphire sample, showing the linear behavior in the edge region, as per Urbach tail model.

where $E = h\nu$ is the light wave energy, T is the temperature, α_0 and E_0 are material specific parameters which can be properly obtained by performing optical transmission measurements at different temperatures and $E_U(T)$ is the Urbach energy, which represents the absorption edge width. [50] As we didn't measure absorption spectra as a function of temperature, we used literature values of E_0 and α_0 parameters. The E_0 parameter is of the order of magnitude of the material's band gap, while α_0 was kept as a free parameter in our analysis. [51]

This exponential increase in the absorption coefficient before the absorption edge is explained as the result of transitions between the tails of the density of states in the valence and the conduction bands. The size and shape of such tails is dependent on the disorder in the crystalline structure and has a strong dependence on temperature. [50, 52]

The GaN layer had a Urbach tail absorption model, while sapphire was treated as a transparent medium. The Urbach energy $E_U(T)$ can be estimated by plotting the transmission data in a $\ln(-\ln T)(E)$ plot[4], as shown in Figure 4.12. The slope of the linear part of such plot is the reciprocal of the Urbach energy: $E_U^{-1} = \frac{\partial \ln \alpha}{\partial h\nu}$. In our n-GaN sample such analysis returned an Urbach energy $E_U = 19(1)$ meV, which matches literature values for GaN at room temperature 10-20 meV. [51, 53]

Once the Urbach energy for the GaN layer was obtained by direct fitting of the data, we proceeded to simulate the transmission spectrum. Our two layers model included a thin GaN layer (5 µm), which made possible the Fabry-Perot interference, and a thick sapphire layer (430 µm), which we modeled as an incoherent layer, i. e. it was set

4 As one can model the effect of absorption on the transmission signal for a layer of d thickness as: $T = \exp(-\alpha d)$. Introducing Equation 4.24 one obtains $T = \exp\left(-\alpha_0 d \exp\left(\frac{E-E_0}{E_U}\right)\right)$.

not to produce interference patterns (using the methods explained in Appendix A).

This choice for the sapphire layer removed the possibility of simulating the high frequency oscillations seen in the NIR region, which are often hard to measure with the experimental apparatus and do not carry significant information on our sample. The addition of such incoherent sapphire model allowed us to closely reproduce the measured transmission spectrum, averaging on such high-frequency oscillations and resulting in an oscillation amplitude which matched the experimental data, unlike models which included thin film interference due to sapphire layer, which instead showed oscillation amplitude in the 60-100 T% range. In this case we consider that in the GaN film a possible loss of coherence and/or optical inhomogeneities as discussed above. To model this aspect we included in our simulations the effect of roughness, as explained in the appendix.

By manually tuning the thickness, roughness and absorption parameters we were able to obtain a simulation which matched most of the features of the experimental spectrum. The main parameters obtained from this simulation are reported in Table 4.5. GaN's film thickness was found to be $5.57(1)\,\mu m$.

The amplitude modulation near the absorption edge could only be reproduced by setting a GaN-sapphire interface roughness of $15.1(5)\,nm$. The high-quality commercial n-GaN thin-film and the polished sapphire substrate were assumed to have no surface roughness and for this reason we decided to assume the RMS roughness for such interfaces to be 0.

FE:LINBO$_3$ ON GAN SAMPLES Once the main features of the substrate's transmission spectrum were understood and modeled, we proceeded to analyze the spectra of three Fe:$LiNbO_3$ on n-GaN samples: N1, N2, N3. Their experimental transmission spectra are shown in Figure 4.13.

In these three spectra we can spot many common features of the n-GaN spectrum, such as the amplitude modulation due to the GaN layer, the absorption edge at 3.4 eV, which matches GaN's band gap. However we can also notice two new features. First we can see a low frequency modulation on the whole transmission spectrum, due to lithium niobate's thin film, of much larger period, compared to GaN one. Secondly, a more intense absorption can be noticed close to the absorption edge.

Absorption of the lithium niobate layer was modeled as an Urbach model. [54] However it should be noted that the GaN edge sets in at longer wavelengths than the $LiNbO_3$ one (energy gap for GaN: 3.4 eV; direct band gap for $LiNbO_3$: 3.93 eV [55]). Thus the lithium niobate

Table 4.5: Parameters used in the simulation of the optical transmission spectra for the n-GaN on sapphire substrate and three Fe:$LiNbO_3$ on n-GaN samples. Film thickness is denoted with d, Urbach energy with E_u, interface roughness with z.

Sample	substrate	N1	N2	N3
d^{GaN} (µm)	5.57(1)	5.57(1)	5.57(1)	5.57(1)
d^{LN} (µm)	/	0.230(5)	0.330(5)	0.250(5)
E_u^{GaN} (meV)	19(1)	17(1)	17(1)	17(1)
E_u^{LN} (meV)	/	150(10)	200(10)	150(10)
α_0^{GaN} ($10^8\,cm^{-1}$)	5.0(5)	16(1)	16(1)	16(1)
α_0^{LN} ($10^7\,cm^{-1}$)	/	3(1)	4(1)	30(2)
E_0^{GaN} (eV)	3.56	3.56	3.56	3.56
E_0^{LN} (eV)	/	4.50	4.50	4.50
$z^{GaN-Al_2O_3}$ (nm)	15.1(1)	15.1(5)	15.1(5)	16.1(5)

edge is most probably not visible in our data, being hidden by the edge of the GaN.

In this simulation, we proceeded to add lithium niobate as a thin film layer on top of the already modeled GaN on sapphire substrate, operating mainly small corrections on lithium niobate's E_u parameter and the α_0 coefficient. The parameters used in the simulations are reported in Table 4.5.

4.3.3 *Results*

Lithium niobate's Urbach energy was found to have values ranging from 150 to 200 meV, higher than values found in literature (80-100 meV). [55] However, as we weren't able to measure lithium niobate's absorption edge directly, this estimation may depend on the choice of other absorption model parameters, such as lithium niobate's absorption edge. This value may vary depending on the Fe concentration, which is a poorly known parameter of our samples. Unfortunately, as lithium niobate's absorption edge is in the GaN absorption region, we were not able to measure it and to estimate total Fe impurity concentration, with the method of [21].

Lithium niobate film thicknesses were found to be in the hundred of nm order of magnitude, with the N1 and N3 samples having comparable thickness of 230(5) and 250(5) nm while the N2 sample was thicker about 330(5) nm. This matches the qualitative trend in RBS measurements (Figure 4.9), where the Nb signal for the P2 sample (deposited in the same sputtering run as the N2) was associated to a wider Nb signal peak compared to P1 and P3 signals, therefore indicating a thicker layer that allows incoming ions to lose more energy before the backscattering event.

Such thicknesses were found to match the period in long range oscillation due to lithium niobate, even though often a phase shift resulted in the simulation not entirely matching the measured spectrum. A similar and more evident phase mismatch behavior affected the GaN high frequency oscillations in N1, N2, N3 sample, although the period of such oscillations was found to match between the data and the simulations. A finer tuning of thickness parameters would probably resolve such differences, even though most of the physical interesting information can be already recovered from the current simulation.

It must be reported that the estimated thin film thickness by this optical method is sensitive on the material's refractive index and this parameter is also reported to change with lithium niobate's composition. [56] For this reason further evaluation of the effect of refractive index changes on the determination of the film thickness in our simulation would set an accurate uncertainty range for this quantity.

The apparent phase shift between our simulation and the experimental data hints at refractive index differences between our material and bulk cLN, whose Sellmeier equation was used for the simulation. As such differences could progressively increase depending on the wavelength, the observed effect would be of a build-up of a phase mismatch.

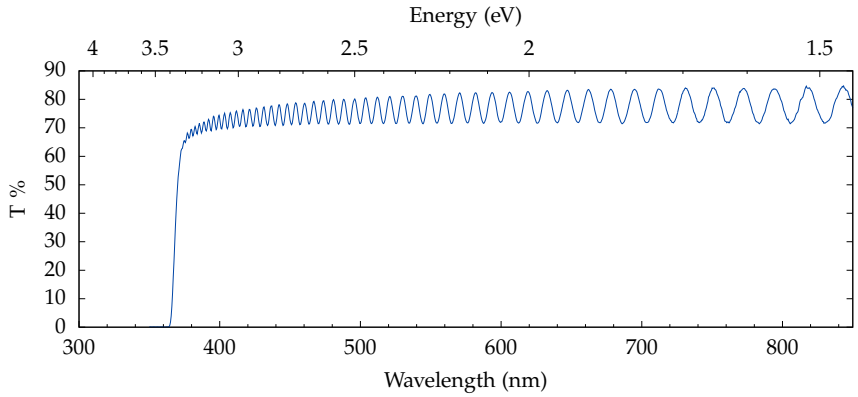

(a) n-GaN on sapphire substrate

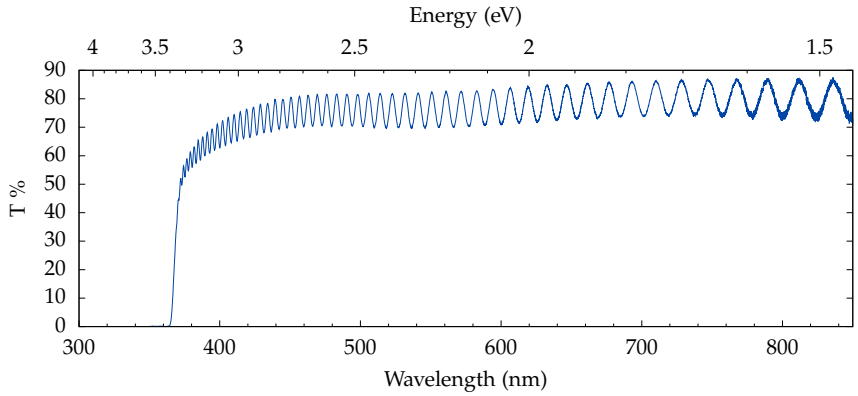

(b) N1 sample

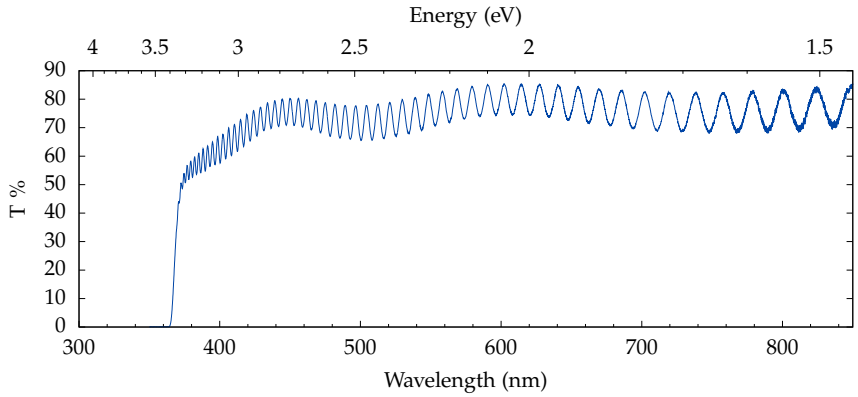

(c) N2 sample

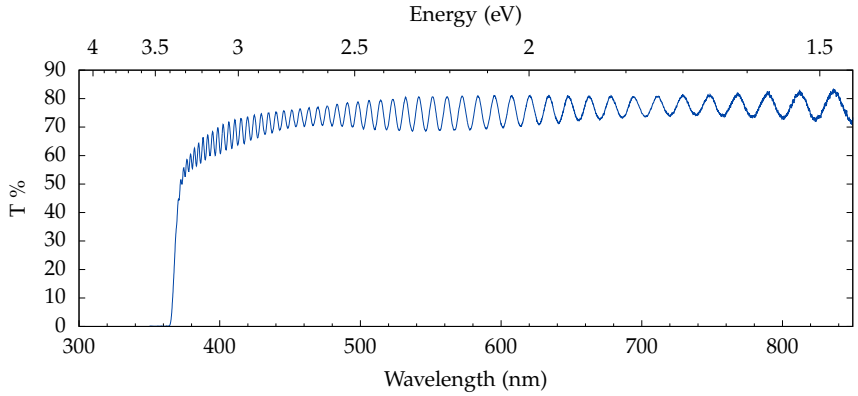

(d) N3 sample

Figure 4.13: Experimental transmission data for a n-GaN on sapphire substrate and three Fe:$LiNbO_3$ samples (N1, N2, N3).

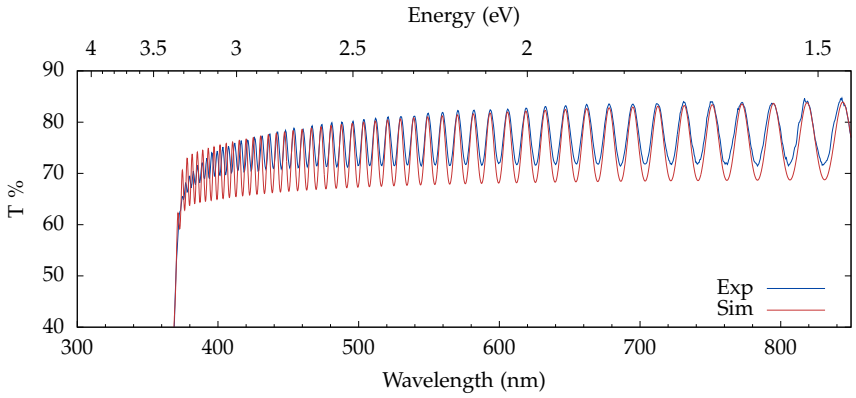

(a) n-GaN on sapphire substrate

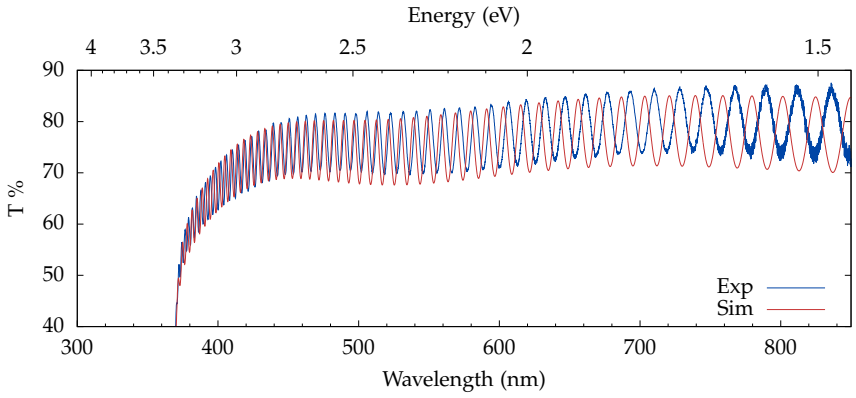

(b) N1 sample

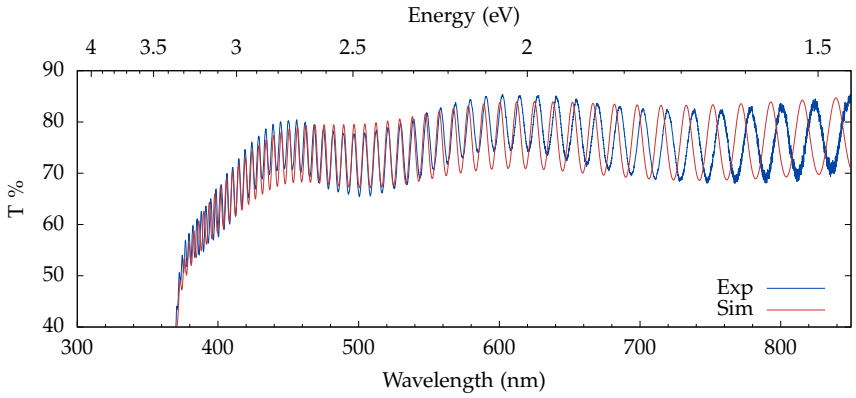

(c) N2 sample

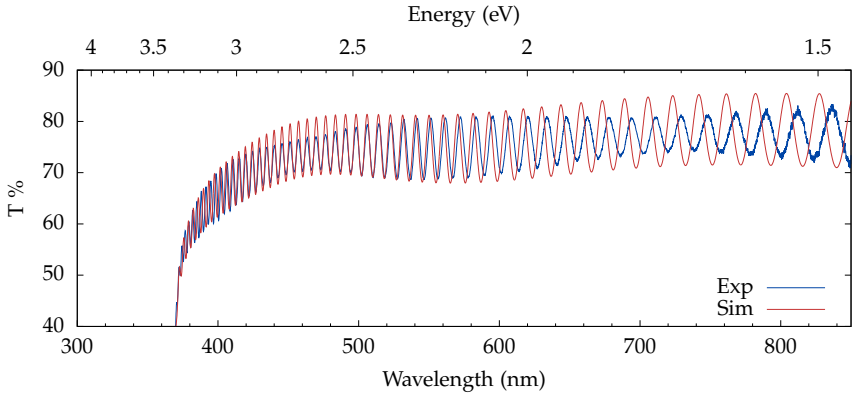

(d) N3 sample

Figure 4.14: Simulated and experimental transmission data for a n-GaN on sapphire substrate and three Fe:$LiNbO_3$ samples (N1, N2, N3).

5

CONCLUSIONS

This thesis work represents several new steps in a broader research project on the study of bulk photovoltaic effect in iron-doped lithium niobate at the nanoscale. The system of our choice, epitaxially grown Fe:$LiNbO_3$ thin films, were characterized for their composition, structural and optical absorption properties.

Our samples were synthesized using Radio Frequency Magnetron Sputtering on $(0\,0\,1)$ GaN on sapphire substrates. The substrate was chosen for the closely matching lattice structure that made epitaxial growth possible. Additionally GaN, a transparent semiconductor, can be doped making it possible to use it as back contact in electrical measurement of the Fe:$LiNbO_3$ photocurrent.

The films were produced experimenting different conditions in the range suggested by previous reports found in literature, exploring different atmosphere compositions and total pressure. Films of thickness of the order of 200 and 300 nm were obtained. Once optimal settings for crystalline thin film deposition will be found, the technique will allow to synthesize films of different thickness by changing the deposition time, allowing to study BPVE at different length scales.

Surface topography studies by Atomic Force Microscopy revealed peculiar features in the form of squared pillars a hundred nm wide with some of them tens of nm high. All of the sample's surface appeared covered in such pattern. Such features could be growth facets, result of the expected Volmer-Weber type of growth.

At the same total pressure, a decrease in the oxygen pressure resulted in faster growth and often in higher pillars, showing the same squared pattern on the rest of the surface. Reducing the total pressure while keeping similar Ar:O_2 ratios as before resulted in a completely different surface morphology. A smooth surface was found without any sign of the squared pattern as before. We think this may be due to a re-sputtering phenomenon eroding part of the deposited film.

High Resolution X-Ray Diffractometry showed that all films have the crystalline structure of lithium niobate and have good crystalline quality as testified by the narrow Bragg peaks. Our film crystal structure was studied and compared to the bulk lithium niobate one. We measured a reduction of its cell around -8% in the interface plane and of -7% along perpendicular to it. Such deformation can be due both to epitaxial growth strain due to the mismatch between GaN and $LiNbO_3$ lattices and to a different composition of the films.

Compositional analysis was performed on the samples to measure their Nb and Li content. Rutherford Backscattering Spectrometry measurements were employed to measure the Nb concentration in the films and showed samples having a concentration close the the congruent value, with some differences depending on the deposition conditions.

Nuclear Reaction Analysis measurements were performed to measure the lithium concentration and reported a general lithium deficiency in our sample, around 50% of the congruent value. This is expected as thin films deposited by RF magnetron sputtering are generally reported to be sub-stoichiometric. A role can also be ascribed by the strong Fe doping of our samples, which needs to be better investigated. The deposition parameters will have to be further tuned in the future to obtain films with composition matching the bulk one.

Additionally, RBS channeling measurements were performed and showed no significant differences in yield for ion beams oriented along the crystal axis or randomly oriented. This hints to the presence of a significant amount of structural defects is present in the Fe:$LiNbO_3$ film. Since from HR X-ray diffraction data we have evidence of a highly oriented lattice with narrow diffraction peaks, a possible explanation for this observation is that our film is characterized by a high density of threading dislocations favoring the beam de-channeling in the lithium niobate film.

The samples' absorption properties were characterized by optical absorption spectroscopy in the UV-Vis range. The transmittance data was analyzed by means of simulations based on the Transfer Matrix Method, which allowed to model the heterostructure's optical transmission. The implemented method allowed to include the effect of thin-films, thick substrates and non homogeneities in the interfaces between them.

Using such methods it was possible to accurately model the substrate optical behavior and characterize thin film thicknesses based on an optical method. Its use on our Fe:$LiNbO_3$ samples however revealed differences between the film refractive index compared to standard lithium niobate of congruent composition. This is almost certainly due to the strongly sub-congruent composition of our films. As a

consequence the agreement between our data and the simulation is only semi-quantitative. Still the code is now available for precise measurement as soon as samples with the appropriate composition will be produced.

This work represents a step in the understanding of the optimal deposition conditions for Fe:$LiNbO_3$ thin-films on GaN, in a broader project to study the photovoltaic properties of this material. This thesis tested a set of characterization techniques for this specific system, providing a toolset for further studies.

As this thesis evidenced, the strong lithium deficiency of films deposited in the explored deposition conditions must be resolved, by changing the deposition atmosphere or by performing co-sputtering with a suitable target such as LiO_2.

A follow up work to this thesis would include a study of the effect of the sputtering conditions and thin film thicknesses on the film's properties studied in this thesis, such as its composition, surface morphology, crystalline structure and strain and absorption properties.

Once the synthesis of Fe:$LiNbO_3$ thin films is mastered, electrical properties of the system could be investigated, making it possible to study the photocurrents originating from BPVE at different wavelengths and the effect of a reduced size on the photovoltaic charge extraction.

A

TRANSFER MATRIX METHOD

In thin film research, optical absorption spectroscopy is an useful tool to probe many properties of the material such as film thickness or absorption by specific impurities. In such experiments, the sample is illuminated by a monochromatic light beam and the light intensity after the sample is measured. This intensity is normalized by a baseline measurement of the light source intensity without the sample and this way the absolute transmission coefficient is obtained.

To understand this data, models of the light propagation through the sample are developed, starting from Fresnel's laws which express how a light wave crosses an interface between two different optical media, splitting in transmitted and reflected components. In general, the light wave can undergo multiple reflections in the material and, if light's coherence length is longer than the thickness of the layer it can interfere with its reflections, as in a Fabry-Perot interferometer.

Models to compute the amplitude of light waves crossing single layers can be readily developed. However, when the samples are multilayered structures, the problem becomes increasingly harder as one would have to sum up the intensity of multiply reflected beams in different media.

The problem of developing a model of the transmittance or reflectance spectrum of a multilayer structure, such the heterostructures synthesized in this thesis can be easily solved with the introduction of the *Transfer Matrix Method* (TMM). [47]

The core idea of the method is to define a 2D vector with the forward and backward propagating complex electric field amplitudes composing the light wave, where E_i^+ represents the forward propagating wave and E_i^- the backward propagating one. As the relationship between the light wave field amplitudes at the sides of an interface or of a layer is found to be linear, one can encode them in 2x2 matrices, one for each interface or layer crossed. Matrix multiplication of such matrices elegantly takes into account all of the possible combinations

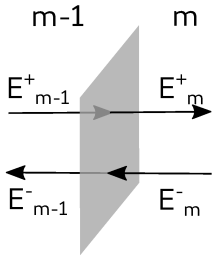

Figure A.1: Schematic showing the notation for the forward (+) and backward (−) propagating light wave field amplitudes at an interface between two different media, labeled $m-1$ and m.

of reflections and transmissions and results in a single transfer matrix T which models the whole multilayer's optical response, so that the light amplitude after the N-th layer can be computed as:

$$\begin{pmatrix} E_0^+ \\ E_0^- \end{pmatrix} = T_{0/N+1} \begin{pmatrix} E_{N+1}^+ \\ E_{N+1}^- \end{pmatrix} \tag{A.1}$$

The effect of an interface between the medium $m-1$ and the next medium m to the forward and backward propagating light waves field amplitudes E^+ and E^- is encoded in the two equations:

$$\begin{cases} E_m^+ = & E_{m-1}^+ t_{m-1,m} + E_m^- r_{m,m-1} \\ E_{m-1}^- = & E_{m-1}^+ r_{m-1,m} + E_m^- t_{m,m-1} \end{cases} \tag{A.2}$$

where $r_{i,j}$ and $t_{i,j}$ are Fresnel complex amplitude reflection and transmission coefficients. We can rewrite them in the matrix equation form as:

$$\begin{pmatrix} E_{m-1}^+ \\ E_{m-1}^- \end{pmatrix} = \frac{1}{t_{m-1,m}} \begin{bmatrix} 1 & -r_{m,m-1} \\ r_{m-1,m} & t_{m,m-1}t_{m-1,m} - r_{m,m-1}r_{m-1,m} \end{bmatrix} \begin{pmatrix} E_m^+ \\ E_m^- \end{pmatrix} = \tag{A.3}$$

$$= D_{m-1}^{-1} D_m \begin{pmatrix} E_m^+ \\ E_m^- \end{pmatrix} \tag{A.4}$$

The effect of crossing a layer of a certain medium of complex refractive index n_m and thickness d_m for the light wave field $E(\mathbf{x}) = E\exp\{i\mathbf{kx} - \omega t\}$ will be a phase shift $\delta_m = 2\pi/\lambda n_m d_m$:

$$\begin{pmatrix} E_m^+ \\ E_m^- \end{pmatrix} = \begin{bmatrix} \exp(-i\delta_m) & 0 \\ 0 & \exp(i\delta_m) \end{bmatrix} \begin{pmatrix} E_m'^+ \\ E_m'^- \end{pmatrix} = \tag{A.5}$$

$$= P_m \begin{pmatrix} E_m^+ \\ E_m^- \end{pmatrix} \tag{A.6}$$

where E_m and E_m' represent the light wave field at opposite interfaces delimiting the layer.

This formalism is valid both for transparent and absorbing media. To account for absorption, one simply has to include the complex part of the refractive index $n = n_{re} + i\, n_{im}$, which will result in a damping of the field amplitude of the light wave crossing the layer. The complex part of the material's refractive index can be computed from it absorption coefficient as: $k = \alpha \frac{\lambda}{4\pi}$.

Recursive use of such matrix relations allows to link the amplitude in the first medium, E_0, to the one in the last medium E_{N+1}, which are the fields on which the measured transmission coefficients are defined. The whole multilayer will be modeled by a transfer matrix obtained from matrix multiplication of matrices for intermediate layers and interfaces.

$$\begin{pmatrix} E_0^+ \\ E_0^- \end{pmatrix} = D_0^{-1} \left[\prod_{m=1}^{N} D_m P_m D_m^{-1} \right] D_{N+1} \begin{pmatrix} E_{N+1}^+ \\ E_{N+1}^- \end{pmatrix} = \tag{A.7}$$

$$= \begin{bmatrix} T_{11} & T_{12} \\ T_{21} & T_{22} \end{bmatrix} \begin{pmatrix} E_{N+1}^+ \\ E_{N+1}^- \end{pmatrix} \tag{A.8}$$

$$\tag{A.9}$$

The complex refraction and transmission amplitude coefficients for the multilayer can be easily written as a function of the components of the multilayer transfer matrix, i. e.:

$$t = t_{0,N+1} = \frac{E_{N+1}'^+}{E_0'^+} = \frac{1}{T_{11}} \tag{A.10}$$

The measured transmittance (T) and reflectance (R) can be computed as the square of the magnitude of the complex *field amplitude* transmission and reflection coefficients and are defined as ratios between the reflected or transmitted *field intensities* and the incident one.

Once the basic formalism is developed, two modifications can be devised to extend the formalism to model partial or total incoherence, that is the loss of coherence of the propagating light waves, resulting in reduced or absent interference from certain layers.

PARTIAL INCOHERENCE Surface or interface roughness or a perturbation on the layer's refractive index can reduce the coherence of the propagating light, resulting in a reduction of the interference amplitude in the measured signal. This is especially relevant for smaller wavelengths, as field oscillations happen at lengths scales comparable to the roughness length scale.

To account for surface roughness of an interface in TMM one can modify the Fresnel coefficients relative to that interface, by introducing multiplicative factors that represent the phase differences in the reflected and transmitted beams that result from a Gaussian distri-

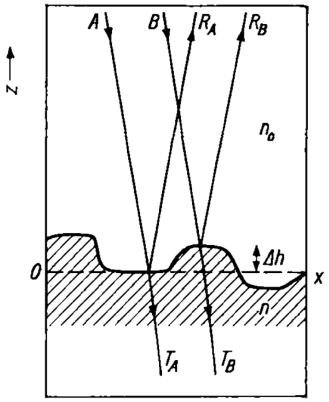

Figure A.2: Schematic showing reflection and transmission of light waves at a rough interface and illustrating the source of the optical path differences between reflected or transmitted waves. From [57]

bution of irregularities of height Δh and RMS height z. [57] Due to surface roughness, optical path differences form between incident and reflected waves (Figure A.2) and can be computed as $\Delta l_r = 2\Delta h\ n_0$. This results in the phase difference $\Delta\Phi_r = 4\pi\Delta h\ n_0/\lambda_0$, where n_0 is the medium's refractive index and λ_0 is the light wave wavelength. The effect of a Gaussian distribution of irregularities of Δh height and z RMS height on the complex reflection coefficients is:

$$r_{m-1,m} = r^{(0)}_{m-1,m} \exp\left[-2\left(\frac{2\pi\ z\ n_{m-1}}{\lambda_0}\right)^2\right] = \alpha r^{(0)}_{m-1,m} \qquad \text{(A.11)}$$

where $r^{(0)}_{m-1,m}$ is the complex reflection coefficient at smooth interface.

In a similar way roughness can induces a phase difference between transmitted waves, $\Phi_t = 2\pi\Delta h(n - n_0)/\lambda_0$, which results in a modification of the complex transmission coefficients as:

$$t_{m-1,m} = t^{(0)}_{m-1,m} \exp\left[-\frac{1}{2}\left(\frac{2\pi\ z\ (n_m - n_{m-1})}{\lambda_0}\right)^2\right] = \gamma t^{(0)}_{m-1,m} \qquad \text{(A.12)}$$

TOTAL INCOHERENCE Often in optical transmission spectroscopy is necessary to model the optical behavior of a thick substrate. If we were to employ the conventional TMM, as explained in the previous paragraphs, our simulation of the transmission spectra would include high frequency oscillations due to thin-film interference from the thick substrate, as the period of such oscillations is inversely proportional to the layer's thickness.

Such high frequency modulation of the signal is often not measured, due to interference destroying effects such as non planarity of the two sides of the substrate, or limited sensitivity of the spectrophotometer.

However, models neglecting the substrate layer often result in simulations which do not match the experimental data, as for example the Fabry-Perot interference amplitude is found to oscillate in a wider range of values compared to the measured data.

To account for this case, a modified TMM was devised, to specifically account for thick layers which do not show thin-film interference behavior.

Let's take the general example of an incoherent layer surrounded by thin film layers on both sides. The idea is to model all the thin film layers using conventional TMM, obtaining an effective transfer matrix for the layers up to the incoherent one and another one for the layers after the incoherent one.

The idea is to replace the complex *amplitude* reflection and transmission coefficients in such matrices by their square amplitude and obtain *intensity matrices*, which directly express the change in the intensity and not in the amplitude of the light wave field. Matrix multiplication of such intensity matrices cannot result in interference originating from the incoherent layer and realizes the addition of field intensities as in a totally incoherent layer.

The intensity matrices for the multilayer including a thick incoherent layer m are computed as:

$$T^{incoh}_{0,N+1} = T^{int}_{0,m}\ P^{int}_{m}\ T^{int}_{m,N+1} \tag{A.13}$$

where the three matrices are computed as:

$$T^{int}_{0,m} = \frac{1}{|t_{0,m}|^2}\begin{bmatrix} 1 & -|r_{m,0}|^2 \\ |r_{0,m}|^2 & (|t_{m,0}t_{0,m}|^2 - |r_{m,0}r_{0,m}|^2) \end{bmatrix} \tag{A.14}$$

$$P^{int}_{m} = \begin{bmatrix} |\exp(-i\delta_m)|^2 & 0 \\ 0 & |\exp(i\delta_m)|^2 \end{bmatrix} \tag{A.15}$$

$$T^{int}_{m,N+1} = \frac{1}{|t_{m,N+1}|^2}\begin{bmatrix} 1 & -|r_{m,N+1}|^2 \\ |r_{m,N+1}|^2 & (|t_{N+1,m}t_{m,N+1}|^2 - |r_{N+1,m}r_{m,N+1}|^2) \end{bmatrix} \tag{A.16}$$

To analyze the transmission spectra for our Fe:$LiNbO_3$ on a GaN on sapphire substrate the three formulations of the TMM will be employed jointly. By tuning the thickness, absorption parameters of the layers and the roughness of the interfaces it was possible to develop accurate models which closely matched the experimental data.

BIBLIOGRAPHY

[1] Sven Rühle. "Tabulated values of the Shockley–Queisser limit for single junction solar cells". In: *Solar Energy* 130 (June 2016), pp. 139–147. DOI: 10.1016/j.solener.2016.02.015.

[2] A. Zenkevich et al. "Giant bulk photovoltaic effect in thin ferroelectric BaTiO 3 films". In: *Physical Review B* 90.16 (Oct. 28, 2014), p. 161409. DOI: 10.1103/PhysRevB.90.161409.

[3] Shankari Nadupalli, Jens Kreisel, and Torsten Granzow. "Increasing bulk photovoltaic current by strain tuning". In: *Science Advances* 5.3 (Mar. 2019), eaau9199. DOI: 10.1126/sciadv.aau9199.

[4] Charles Paillard et al. "Photovoltaics with Ferroelectrics: Current Status and Beyond". In: *Advanced Materials* 28.26 (July 2016), pp. 5153–5168. DOI: 10.1002/adma.201505215.

[5] A. M. Glass, D. von der Linde, and T. J. Negran. "High-voltage bulk photovoltaic effect and the photorefractive process in $LiNbO_3$". In: *Applied Physics Letters* 25.4 (Aug. 15, 1974), pp. 233–235. DOI: 10.1063/1.1655453.

[6] R. S. Weis and T. K. Gaylord. "Lithium niobate: Summary of physical properties and crystal structure". In: *Applied Physics A Solids and Surfaces* 37.4 (Aug. 1985), pp. 191–203. DOI: 10.1007/BF00614817.

[7] Tatyana Volk and Manfred Wöhlecke. *Lithium niobate: defects, photorefraction and ferroelectric switching*. Springer series in materials science 115. OCLC: ocn233935198. Berlin: Springer, 2008. 247 pp.

[8] V.Ya. Shur. "Lithium niobate and lithium tantalate-based piezoelectric materials". In: *Advanced Piezoelectric Materials*. Elsevier, 2010, pp. 204–238. DOI: 10.1533/9781845699758.1.204.

[9] R. T. Smith and F. S. Welsh. "Temperature Dependence of the Elastic, Piezoelectric, and Dielectric Constants of Lithium Tantalate and Lithium Niobate". In: *Journal of Applied Physics* 42.6 (May 1971), pp. 2219–2230. DOI: 10.1063/1.1660528.

[10] A. W. Warner, M. Onoe, and G. A. Coquin. "Determination of Elastic and Piezoelectric Constants for Crystals in Class (3*m*)". In: *The Journal of the Acoustical Society of America* 42.6 (Dec. 1967), pp. 1223–1231. DOI: 10.1121/1.1910709.

[11] Tomoaki Yamada, Nobukazu Niizeki, and Hiroo Toyoda. "Piezoelectric and Elastic Properties of Lithium Niobate Single Crystals". In: *Japanese Journal of Applied Physics* 6.2 (Feb. 1967), pp. 151–155. DOI: 10.1143/JJAP.6.151.

[12] J. R. Teague, R. R. Rice, and R. Gerson. "High-frequency dielectric measurements on electro-optic single crystals". In: *Journal of Applied Physics* 46.7 (July 1975), pp. 2864–2866. DOI: 10.1063/1.322031.

[13] K. K. Wong, Institution of Electrical Engineers, and INSPEC (Information service), eds. *Properties of lithium niobate*. EMIS datareviews series no. 28. OCLC: ocm48884959. London: INSPEC/Institution of Electrical Engineers, 2002. 417 pp.

[14] M. Luennemann et al. "Electrooptic properties of lithium niobate crystals for extremely high external electric fields". In: *Applied Physics B: Lasers and Optics* 76.4 (Apr. 1, 2003), pp. 403–406. DOI: 10.1007/s00340-003-1123-9.

[15] E. H. Turner. "High frequency electro-optic coefficients of lithium niobate". In: *Applied Physics Letters* 8.11 (June 1966), pp. 303–304. DOI: 10.1063/1.1754449.

[16] A. Ashkin et al. "Optically-induced refractive index inhomogeneities in $LiNbO_3$ and $LiTaO_3$". In: *Applied Physics Letters* 9.1 (July 1966), pp. 72–74. DOI: 10.1063/1.1754607.

[17] David Emin. "Optical properties of large and small polarons and bipolarons". In: *Physical Review B* 48.18 (Nov. 1, 1993), pp. 13691–13702. DOI: 10.1103/PhysRevB.48.13691.

[18] N. Iyi et al. "Comparative study of defect structures in lithium niobate with different compositions". In: *Journal of Solid State Chemistry* 101.2 (Dec. 1992), pp. 340–352. DOI: 10.1016/0022-4596(92)90189-3.

[19] A. P. Wilkinson, A. K. Cheetham, and R. H. Jarman. "The defect structure of congruently melting lithium niobate". In: *Journal of Applied Physics* 74.5 (Sept. 1993), pp. 3080–3083. DOI: 10.1063/1.354572.

[20] A. Zaltron et al. "Iron site location in Fe-diffused lithium niobate crystals by combined RBS-PIXE-NRA analysis". In: *Nuclear Instruments and Methods in Physics Research Section B: Beam Interactions with Materials and Atoms* 275 (Mar. 2012), pp. 11–15. DOI: 10.1016/j.nimb.2011.12.021.

[21] Maria Vittoria Ciampolillo et al. "Quantification of Iron (Fe) in Lithium Niobate by Optical Absorption". In: *Applied Spectroscopy* 65.2 (Feb. 2011), pp. 216–220. DOI: 10.1366/10-06015.

[22] O. F. Schirmer, M. Imlau, and C. Merschjann. "Bulk photovoltaic effect of $LiNbO_3$:Fe and its small-polaron-based microscopic interpretation". In: *Physical Review B* 83.16 (Apr. 12, 2011), p. 165106. DOI: 10.1103/PhysRevB.83.165106.

[23] V. M. Fridkin. "Bulk photovoltaic effect in noncentrosymmetric crystals". In: *Crystallography Reports* 46.4 (July 2001), pp. 654–658. DOI: 10.1134/1.1387133.

[24] A. Sanson et al. "Polaronic deformation at the $Fe^{2+/3+}$ impurity site in Fe:$LiNbO_3$ crystals". In: *Physical Review B* 91.9 (Mar. 17, 2015), p. 094109. DOI: 10.1103/PhysRevB.91.094109.

[25] Giulio Favaro. "Fabrication and characterization of photogalvanic quantum wells". Master Thesis. Padova, Italia: Università degli Studi di Padova, Sept. 2019. 70 pp.

[26] M. P. Sumets, V. A. Dybov, and V. M. Ievlev. "LiNbO3 films: Potential application, synthesis techniques, structure, properties". In: *Inorganic Materials* 53.13 (Dec. 2017), pp. 1361–1377. DOI: 10.1134/S0020168517130015.

[27] Maxim Sumets. *Lithium Niobate-Based HeterostructuresSynthesis, properties and electron phenomena*. IOP Publishing, 2018. DOI: 10.1088/978-0-7503-1729-0.

[28] Junhui He. "Highly C-axis oriented LiNbO3 thin film on amorphous SiO2 buffer layer and its growth mechanism". In: *Chinese Science Bulletin* 48.21 (2003), p. 2290. DOI: 10.1360/03ww0053.

[29] Tsung-Hsin Lee et al. "Investigation of LiNbO3 thin films grown on Si substrate using magnetron sputter". In: *Materials Science and Engineering: B* 136.1 (Jan. 2007), pp. 92–95. DOI: 10.1016/j.mseb.2006.09.001.

[30] S.-K. Park et al. "Properties of LiNbO3 thin film prepared from ceramic Li–Nb–K–O target". In: *Solid State Communications* 111.6 (July 1999), pp. 347–352. DOI: 10.1016/S0038-1098(99)00067-8.

[31] M. Tsirlin. "Influence of gas phase composition on the defects formation in lithium niobate". In: *Journal of Materials Science* 39.9 (May 2004), pp. 3187–3189. DOI: 10.1023/B:JMSC.0000025855.47619.d5.

[32] S. B. Ogale et al. "Pulsed laser deposition of stoichiometric $LiNbO_3$ thin films by using O_2 and Ar gas mixtures as ambients". In: *Journal of Applied Physics* 71.11 (June 1992), pp. 5718–5720. DOI: 10.1063/1.350509.

[33] Coralie Charpentier. "Investigation of deposition conditions and annealing treatments on sputtered ZnO:Al thin films: Material properties and application to microcristalline silicon solar cells." Doctoral thesis. Ecole Polytechnique X, Dec. 2012.

[34] Peter J. Hansen et al. "LiNbO[sub 3] thin film growth on (0001)-GaN". In: *Journal of Vacuum Science & Technology B: Microelectronics and Nanometer Structures* 23.1 (2005), p. 162. DOI: 10.1116/1.1850106.

[35] Simone Sanna and Wolf Gero Schmidt. "GaN growth on $LiNbO_3$ (0001) - a first-principles simulation". In: *physica status solidi (c)* 7.7 (June 10, 2010), pp. 2272–2274. DOI: 10.1002/pssc.200983649.

[36] Neil W. Ashcroft and N. David Mermin. *Solid state physics*. New York: Holt, Rinehart and Winston, 1976. 826 pp.

[37] M A Moram and M E Vickers. "X-ray diffraction of III-nitrides". In: *Reports on Progress in Physics* 72.3 (Mar. 1, 2009), p. 036502. DOI: 10.1088/0034-4885/72/3/036502.

[38] W. J. Bartels. "Characterization of thin layers on perfect crystals with a multipurpose high resolution x-ray diffractometer". In: *Journal of Vacuum Science & Technology B: Microelectronics and Nanometer Structures* 1.2 (1983), p. 338. DOI: 10.1116/1.582553.

[39] S.G Malhotra et al. "Analysis of thin film stress measurement techniques". In: *Thin Solid Films* 301.1 (June 1997), pp. 45–54. DOI: 10.1016/S0040-6090(96)09569-7.

[40] D. Shilo, E. Lakin, and E. Zolotoyabko. "Comprehensive strain analysis in thin films based on high-resolution x-ray diffraction: Application to implanted $LiNbO_3$". In: *Physical Review B* 63.20 (May 3, 2001), p. 205420. DOI: 10.1103/PhysRevB.63.205420.

[41] Terry L. Alford, Leonard C. Feldman, and James W. Mayer. *Fundamentals of nanoscale film analysis*. OCLC: ocn124465046. New York, N.Y. ; London: Springer, 2007. 336 pp.

[42] James F. Ziegler, M.D. Ziegler, and J.P. Biersack. "SRIM – The stopping and range of ions in matter (2010)". In: *Nuclear Instruments and Methods in Physics Research Section B: Beam Interactions with Materials and Atoms* 268.11 (June 2010), pp. 1818–1823. DOI: 10.1016/j.nimb.2010.02.091.

[43] M. Levy et al. "Fabrication of single-crystal lithium niobate films by crystal ion slicing". In: *Applied Physics Letters* 73.16 (Oct. 19, 1998), pp. 2293–2295. DOI: 10.1063/1.121801.

[44] A.F. Gurbich. "Evaluated differential cross-sections for IBA". In: *Nuclear Instruments and Methods in Physics Research Section B: Beam Interactions with Materials and Atoms* 268.11 (June 2010), pp. 1703–1710. DOI: 10.1016/j.nimb.2010.02.011.

[45] F Agulló-López. *Insulating Materials for Optoelectronics: New Developments*. World Scientific, Nov. 1995. DOI: 10.1142/2720.

[46] I. Golicheff, M. Loeuillet, and Ch. Engelmann. "Determination des fonctions d'excitation des reactions ^{19}F(p, α_0)^{16}O et ^{7}Li(p, α_0)^{4}He entre 150 et 1800 keV: Application a la mesure des concentrations superficielles de lithium et de fluor, data retrieved from the IBANDL database, IAEA, 2019 at http://www-nds.iaea.org/ibandl/." In: *Journal of Radioanalytical Chemistry* 22.1 (Mar. 1974), pp. 113–129. DOI: 10.1007/BF02518097.

[47] Charalambos C. Katsidis and Dimitrios I. Siapkas. "General transfer-matrix method for optical multilayer systems with coherent, partially coherent, and incoherent interference". In: *Applied Optics* 41.19 (July 1, 2002), p. 3978. DOI: 10.1364/AO.41.003978.

[48] Marvin J. Weber. *Handbook of optical materials*. The CRC Press laser and optical science and technology series. Boca Raton: CRC Press, 2003. 512 pp.

[49] David E. Zelmon, David L. Small, and Dieter Jundt. "Infrared corrected Sellmeier coefficients for congruently grown lithium niobate and 5 mol% magnesium oxide –doped lithium niobate". In: *Journal of the Optical Society of America B* 14.12 (Dec. 1, 1997), p. 3319. DOI: 10.1364/JOSAB.14.003319.

[50] Ihor Studenyak, Mladen Kranjec, and Mykhailo Kurik. "Urbach Rule in Solid State Physics". In: *International Journal of Optics and Applications* 4.3 (2014), pp. 76–83. DOI: 10.5923/j.optics.20140403.02.

[51] S. Chichibu et al. "Urbach–Martienssen tails in a wurtzite GaN epilayer". In: *Applied Physics Letters* 70.25 (June 23, 1997), pp. 3440–3442. DOI: 10.1063/1.119196.

[52] M. V. Kurik. "Urbach rule". In: *Physica Status Solidi (a)* 8.1 (Nov. 16, 1971), pp. 9–45. DOI: 10.1002/pssa.2210080102.

[53] M.A Jacobson et al. "Absorption spectra of GaN: film characterization by Urbach spectral tail and the effect of electric field". In: *Journal of Crystal Growth* 230.3 (Sept. 2001), pp. 459–461. DOI: 10.1016/S0022-0248(01)01246-5.

[54] Süleyman Çabuk and Amirullah Mamedov. "Urbach rule and optical properties of the LiNbO $_3$ and LiTaO $_3$". In: *Journal of Optics A: Pure and Applied Optics* 1.3 (May 1, 1999), pp. 424–427. DOI: 10.1088/1464-4258/1/3/313.

[55] R. Bhatt et al. "Urbach tail and bandgap analysis in near stoichiometric LiNbO3 crystals". In: *physica status solidi (a)* 209.1 (Jan. 2012), pp. 176–180. DOI: 10.1002/pssa.201127361.

[56] U. Schlarb and K. Betzler. "Refractive indices of lithium niobate as a function of wavelength and composition". In: *Journal of Applied Physics* 73.7 (Apr. 1993), pp. 3472–3476. DOI: 10.1063/1.352951.

[57] I. Filiński. "The effects of sample imperfections on optical spectra". In: *Physica Status Solidi (b)* 49.2 (Feb. 1, 1972), pp. 577–588. DOI: 10.1002/pssb.2220490220.